

AMERICAN UNIVERSITY OF BEIRUT

ESTIMATING RIVER DISCHARGE RATE USING
REMOTELY SENSED THERMAL PLUMES

by
RONY JOSEPH NASR

A thesis
submitted in partial fulfillment of the requirements
for the degree of Master of Engineering
to the Department of Civil and Environmental Engineering
of the Faculty of Engineering and Architecture
at the American University of Beirut

Beirut, Lebanon
January 2017

AMERICAN UNIVERSITY OF BEIRUT

ESTIMATING RIVER DISCHARGE RATE USING
REMOTELY SENSED THERMAL PLUMES

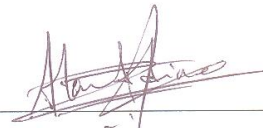
by
RONY J. NASR

Approved by:



Dr. Majdi Abou Najm, Assistant Professor
Department of Civil and Environmental Engineering

Advisor



Dr. Ibrahim Alameddine, Assistant Professor
Department of Civil and Environmental Engineering

Member of Committee



Dr. Elsy Ibrahim, Assistant Professor
Faculty of Engineering, NDU

Member of Committee

Date of thesis defense: January 31, 2017

AMERICAN UNIVERSITY OF BEIRUT

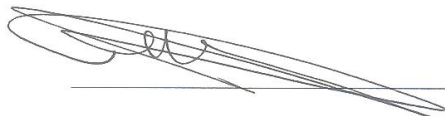
THESIS, DISSERTATION, PROJECT RELEASE FORM

Student Name: Naize Rony Joseph
Last First Middle

Master's Thesis Master's Project Doctoral Dissertation

I authorize the American University of Beirut to: (a) reproduce hard or electronic copies of my thesis, dissertation, or project; (b) include such copies in the archives and digital repositories of the University; and (c) make freely available such copies to third parties for research or educational purposes.

I authorize the American University of Beirut, to: (a) reproduce hard or electronic copies of it; (b) include such copies in the archives and digital repositories of the University; and (c) make freely available such copies to third parties for research or educational purposes
after : **One** --- year from the date of submission of my thesis, dissertation, or project.
Two --- years from the date of submission of my thesis, dissertation, or project.
Three --- years from the date of submission of my thesis, dissertation, or project.



Signature

10-Feb-2017

Date

ACKNOWLEDGMENTS

First and foremost, I would like to thank my thesis advisor Doctor Majdi Abou Najm for his supervision, patient and the enormous trust he gave me. I am grateful to Dr. Ibrahim Alameddine along with Dr. Elsy Ibrahim for their assistantship in the statistical analyses work, their technical support in image treatment techniques and Landsat image exploration procedure and their valuable comments. They allowed this thesis to be my own work, but steered me in the right direction whenever they thought I needed it.

AN ABSTRACT OF THE THESIS OF

Rony Joseph Nasr for Master of Engineering
Major: Environmental and Water Resources Engineering

Title: Estimating river discharge rate using remotely sensed thermal plumes

A methodology for river flow estimation from remotely sensed river thermal plume characteristics is introduced. Rule-based feature extraction tools were utilized to extract geometric characteristics of thermal plumes from 116 Landsat 7 Enhanced Thematic Mapper Plus (ETM+) images of four rivers in Oregon State (Chetco, Coquille, Rogue and Siuslaw Rivers).

The objective was to evaluate the ability of river thermal plume's geometric characteristics (angle, length, deviation angle from the river channel centerline and mean tide level) to predict rivers discharge rate, measured independently through USGS stations. Multiple linear regression models using river plume's geometric characteristics as independent variables accounted for most of the variability in the discharged flow (R^2 : 0.61, 0.54, 0.55, 0.57).

Performance of these models was evaluated using statistical parameters and show satisfactory to good performance. Furthermore, high correlation is found between the river flow and the plume's area and length variables. In fact, evaluation of the adopted plume's area extraction method shows a Heidke Skill Score (HSS) values of 0.80, 0.75, 0.78 and 0.86, respectively for the four rivers.

The proposed method is applied to estimate discharge from rivers with jetties at the mouth of the river.

CONTENTS

ACKNOWLEDGEMENTS	v
ABSTRACT.....	vi
LIST OF ILLUSTRATIONS.....	ix
LIST OF TABLES.....	xi

Chapter

I. INTRODUCTION.....	1
II. STUDY REGION AND DATASETS.....	5
A. Study Area	5
B. Landsat 7 ETM+ imagery	12
C. Landsat imagery and Flow data collection	14
III. METHODOLOGY.....	17
A. Image Processing	19
1. Radiometric Correction	19
2. Landsat ETM+ SLC-OFF gap filling	19
B. Dynamical characterization of the plume	20
C. Delineation of the plume's area	22
D. Evaluation method of the plume's area ENVI extraction method.....	26

E. Determining the plume geometric characteristics	29
F. River discharge linear model	32
IV. RESULTS AND OBSERVATIONS	35
A. Assessment of the “rule-based feature” extraction method in ENVI	35
B. Estimation of discharge rates of the rivers	37
V. DISCUSSION AND CONCLUSION	47
BIBLIOGRAPHY.....	50

Appendix

I. MULTICOLLINEARITY DIAGNOSTIC RESULTS	53
II. CHETCO RIVER MODEL ASSESSMENT PLOTS	54
III. COQUILLE RIVER MODEL ASSESSMENT PLOTS	55
IV. ROGUE RIVER MODEL ASSESSMENT PLOTS	56
V. SIUSLAW RIVER MODEL ASSESSMENT PLOTS	57
VI. DYNAMIC CHARACTERISTICS OF THE PLUME	58
VII CONTINGENCY TABLES	59
VIII MATLAB CODE FOR ELLIPTICAL FIT FOR PLUME SHAPE	60

ILLUSTRATIONS

Figure	Page
1.	General Plan View showing the location of the four rivers in Oregon State. From the top: Siuslaw, Coquille, Rogue and Chetco Rivers 6
2.	Chetco River Mouth plan view from a Google-Earth image. River Mouth width (W) = 80 m. River orientation: 40° N 6
3.	Topographical plan view of Chetco River Mouth showing the location and Chetco Cove..... 7
4.	Rogue River Mouth plan view from a Google-Earth image. River Mouth width (W) = 285m. River orientation: 55° N..... 8
5.	Topographical plan view of Rogue River Mouth showing the location and the direct discharge..... 8
6.	Coquille River Mouth plan view from a Google-Earth image. River Mouth width (W) = 610 m. River orientation: 115° N..... 9
7.	Topographical plan view of Coquille River Mouth showing the location and the direct discharge 9
8.	Siuslaw River Mouth plan view from a Google-Earth image. River Mouth width (W) = 200 m. River orientation: 98° N..... 10
9.	Topographical plan view of Siuslaw River Mouth showing the location and the direct discharge..... 10
10.	Hydrograph of Chetco River on 9/2/2010. The time range is from 12:00 till 20:00. The mean discharge rate is 81.37 m ³ /s, the standard deviation is 1.2 m ³ /s and the percentage of standard deviation from the mean is 1.47%..... 15
11.	Summary of the proposed methodology used to estimate river flow from discharge thermal plume characteristics observed by the Landsat 7 ETM+ images..... 18
12.	Gap filling of Landsat 7 SLC-off scenes using ENVI toolbox feature... 20
13.	Landsat 7 ETM+ image from Rogue River (17/3/2003) showing the plume's area and the excluded part of the plume and the defined boundary limit of the river..... 24

14.	Example of the rule-based feature extraction tool in ENVI to define the scale and merge levels required for the segmentation of the region of interest around the plume's area.....	26
15.	Landsat 7 ETM+ image of Rogue River (23/02/2002) showing the extracted plume areas using the rule-based feature extraction tool in ENVI. Plume area is the combination of both areas marked in green and red.....	26
16.	Landsat 7 ETM+ image of Chetco River (19/1/2001) showing the geometric characteristics of the plume (Plume Length L_m in red till the end of the plume extent, River Centerline in green, and Deviation angle (θ) between the two lines.....	30
17.	Plume shape of Rogue River (29/1/2000) showing in blue the extracted plume from ENVI, in red the ellipse fitting the plume, in black the major axis length representing the plume length L_m and in green the river centerline.....	31
18.	Showing the overlap between the plume and the generated fit ellipse the plume. The assessment performance scores: $F1=0.95$; Accuracy: 0.97	31
19.	Scatter plot of $Q_{estimated}$ (m^3/s) from the linear regression model and Q_{USGS} (m^3/s) from the USGS dataset for Chetco River ($y= 0.86x$) and the 1:1 line in red	40
20.	Scatter plot of $Q_{estimated}$ (m^3/s) from the linear regression model and Q_{USGS} (m^3/s) from the USGS dataset for Coquille River ($y= 0.87x$) and the 1:1 line in red.....	40
21.	Scatter plot of $Q_{estimated}$ (m^3/s) from the linear regression model and Q_{USGS} (m^3/s) from the USGS dataset for Rogue River ($y= 0.89x$) and the 1:1 line in red.....	41
22.	Scatter plot of $Q_{estimated}$ (m^3/s) from the linear regression model and Q_{USGS} (m^3/s) from the USGS dataset for Siuslaw River ($y= 0.93x$) and the 1:1 line in red.....	41

TABLES

Table		Page
1.	Monthly mean discharge rate (m ³ /s) for the four rivers based on the years of record at the rivers gauges (Source: USGS river flows).....	11
2.	Summary of the four rivers hydrological characteristics at the gauge station and the river mouth.....	11
3.	Spectral and spatial resolution of Landsat 7 ETM+ bands.....	12
4.	WRS coordinates of Study Rivers images (path, row), Rivers Mouths locations (Lat, Long) and the corresponding number of images.....	14
5.	Landsat 7 ETM+ SLC-on images (1999-2003) available based on adopted criteria for images selection.....	16
6.	Landsat 7 ETM+ SLC-off images (2003-2015) available based on adopted criteria for images selection.....	16
7.	Shown the description of the parameters needed for the river plume's area definition.....	25
8.	Example of a contingency table showing the nomenclature of the different relations.....	27
9.	Contingency table of plume area classification between Manual and ENVI definitions from Coquille River image dated in 19/12/1999.....	36
10.	Summary of the contingency tables skill scores for the four rivers.....	37
11.	Summary of the initial/final multiple linear regression models of Chetco River.....	38
12.	Summary of the initial/final multiple linear regression models of Coquille River.....	39
13.	Summary of the initial/final multiple linear regression models of Rogue River.....	39
14.	Summary of the initial/final multiple linear regression models of Siuslaw River.....	40
15.	Final multiple linear regression models statistics of the four rivers based on the MATLAB automated method.....	40
16.	Final models equations of the four rivers using the significant parameters of each river.....	40

17.	Final multiple linear regression models statistics of the four rivers based on the manual method.....	40
18.	Estimated discharges v/s measured discharges linear regression lines of the four rivers.....	41
19.	Summary of reported RMSE, RSR, NSE and PBIAS values from the rivers final models.....	43
20.	Reported performance rating of the statistical parameters (RSR, NSE and PBIAS).....	43
21.	Summary of cross validation assessment and model prediction power calculations.....	44

CHAPTER I

INTRODUCTION

Quantifying rivers' discharge is key for a wide spectrum of water resources management application including planning, flood protection, mitigation of contamination, and environmental assessment. Traditionally, in situ gauge measurements are considered the standard technique to quantify river flows. While gauged basins are relatively common in the developed world, the majority of rivers in developing countries remain ungauged. The lack of river flow data presents a major challenge to modelers working on ungauged basins, particularly in terms of model calibration (Birkinshaw et al., 2014; Bjerklie et al., 2005). Recent efforts to mitigate such a challenge and compensate the lack of in-situ measurements in ungauged basins explored the use of remote sensing via satellite-based imagery (Bjerklie et al., 2005; Osadchiev, 2015).

Space-borne imagery not only crosses the political boundary limitation (a major challenge to trans-boundary river basins), but can also bring in cost-effective methods of prediction in ungauged basins around the world. Among the many satellite systems that are used for the study of surface water is the Landsat system. The resolution of the Landsat sensor makes it highly suitable to analyze or evaluate freshwater discharge plume characteristics (Jabbar et al., 2013) and assess river discharge plumes into the sea (Fernandez et al., 2014).

Indirect methods based on remote sensing technique offer the possibility of partially replacing lengthy and expensive direct discharge measurements (Barrett, 1998; Birkinshaw et al., 2014). Several indirect methods of quantifying river discharge based on hydrological modeling and altimetry measurements have been developed (Birkinshaw et al., 2014; Hirpa et al., 2013; Sun et al., 2010), and many others since the 1980s (Dinnel et al., 1990; Kaufman & Adams, 1981).

These methodologies are based on Manning's principle to estimate daily river discharge at an ungauged site from river channel stage level, slope and width detected remotely via satellites images. However, although very good results were obtained with these methods, some limitations restraint their applications, including the need for additional atmospheric or hydrological information such as river bed morphology and bathymetry (Miller et al., 2014; Sun et al., 2010). Furthermore, the spatial resolution of satellite sensors (Birkett et al., 2002), and the absence of required hydrological information (Enjolras et al., 2006) pause major challenges to their application, particularly to small-size rivers with relatively narrow channels.

A different way to deduce river characteristics is by looking at river plumes. The force and momentum injection of river discharge propagates the river plume onto the near-shore shelf, and expands into large areas which can extend for several kilometers (Jirka et al., 1981). The shape and characteristics of river plume can be related to a number of factors including magnitude and direction of wind stress, ocean current, discharge characteristics, bathymetry and tidal effects (Jones et al., 2007). Cole and Hetland (2016) indicated a coarsely linear relationship between plume surface area A_{plume} and river flow, that is, $A_{\text{plume}} \sim c_A^{-1} Q$, where $c_A \sim 6.7 \cdot 10^{-6} \text{ m} \cdot \text{s}^{-1}$.

Richard W Garvine (1995) described the discharged plume dynamics and its relationship with different flow characteristics, including discharge velocity, temperature differential, momentum, and relative buoyancy. Moreover, Jones et al. (2007), Richard W Garvine (1995) among others categorized the plume fields into near and far field areas in which the characteristics of the plume and its interaction with the discharge conditions (like flow rate, velocity, salinity, water quality, temperature) and the receiving body conditions (like tides currents, winds, temperature) differ. The spreading of river plumes in the near-field and far field areas was further studied by F. Chen et al. (2009), Kaufman and Adams (1981), Robert D Hetland and MacDonald (2008) and others by means of numerical models or assessment of remotely sensed images.

Most of the plumes can be differentiated from ambient seawater by satellite sensors because of the difference in color, turbidity, or salinity. In fact, some plumes can be mapped with airborne scanning microwave radiometers and satellite Thermal Infra-Red (TIR) sensors (Burrage et al., 2008), deeming satellites-based thermal infrared sensors very effective for observing coastal plumes (Thomas et al., 2002b) and to assess thermal effluent impacts on water quality (Mustard et al., 1999). While many of these characteristics, remotely sensed by satellite sensors, have been studied such as turbidity (Donald R Johnson et al., 2003; Kaya et al., 2006), total suspended sediments (Coyne et al., 2005; Tilburg et al., 2011), and thermal properties (Mustard et al., 1999), this study highlights on the thermal properties of the discharge plume.

In this article, we present a method for estimating river discharge rate from the buoyant thermal plume formed by the river discharge into water bodies like seas, lakes or oceans. The research consists of temporally monitoring the thermal discharged plumes of four rivers (1999-2015), in Oregon State, during the winter and spring seasons when the river flow is at its maximum levels, with the purpose of estimating the river discharge rate from detected thermal plume area, its geometric characteristics and the corresponding mean tide level. Thermal bands of Landsat 7 ETM+ images were used to retrieve the thermal plume area of the discharge flow using ENVI.

CHAPTER II

STUDY REGION AND DATASETS

A. Study Area

The study region is located on the western coastline of the United States (USA), along the State of Oregon. Four rivers discharging into the Pacific Ocean were chosen: Chetco, Rogue, Coquille and Siuslaw rivers (see Figure 1). These rivers are located in watersheds of similar meteorological, hydrological, morphological characteristics.

The four rivers are situated at an interface between the Pacific Ocean and the Klamath mountains of Oregon. The weather is predominately a product of the moisture laden marine air masses, moving over the rugged and abrupt topography of the Klamath Mountains. This combination of geographical location and topography produces a maritime climate of cool summers and mild, wet winters. Furthermore, the four rivers discharge direct jet into the ocean through river mouth inserted between two breakwaters. Tables 1 and 2 show a summary of the four rivers characteristics.

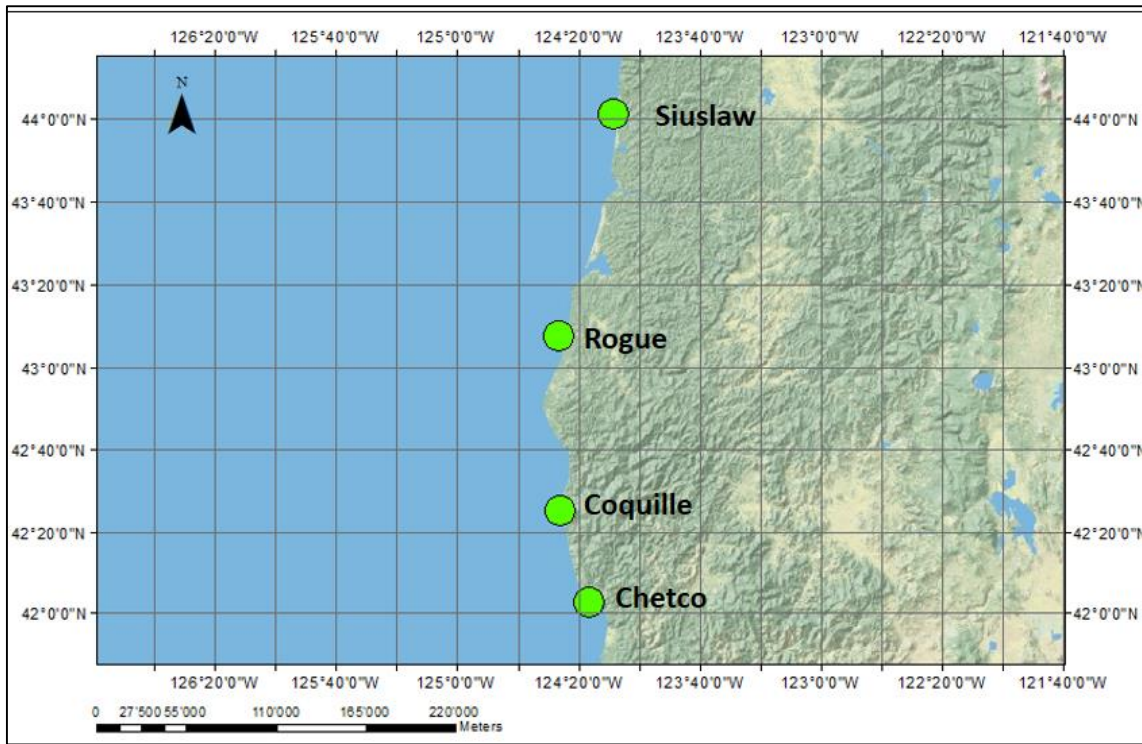


Figure 1: General Plan View showing the location of the four rivers in Oregon State. From the top: Siuslaw, Coquille, Rogue and Chetco Rivers.

The Chetco River has a mean discharge rate of about $64 \text{ m}^3/\text{s}$, a catchment area of 912 km^2 and a length of 90 km . The river enters the Chetco estuary ($413,000 \text{ m}^2$) through a relatively narrow mouth “W”, approximately 80 m , flanked by two jetties, resulting in a discrete point of entry (Figure 2 and 3). The steep gradient of the Chetco river bed restricts the extent of tides and mountainous terrain limits the size of the estuary. Despite this, the lower 5.5 Km of the Chetco River are subject to tidal influences, thus

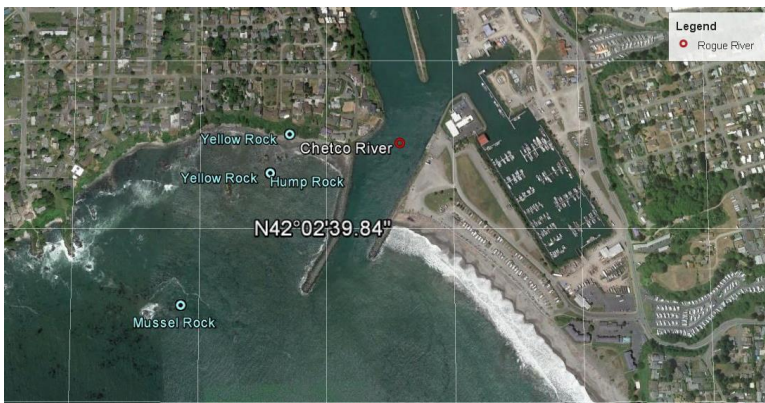


Figure 2: Chetco River Mouth plan view from a Google-Earth image. River Mouth width (W) = 80 m . River orientation: 40° N

impacting the estuary which contains around 10% tidal wetland. The tidal range between mean lower low water (m.l.l.w) and mean higher high water (m.h.h.w) is 2 m and

the extreme tidal range is 4 m (NOAA, 2015). A depth of approximately 5 m is maintained at the entrance of the river and in the navigation channel (*Natural Resources of Chetco Estuary, 1979*).

Flow in Chetco River is monitored by the United States Geological Survey (USGS) at a stream gauge 16 km from the river mouth (RM) northeast of Brookings (*Natural Resources of Chetco Estuary, 1979*).

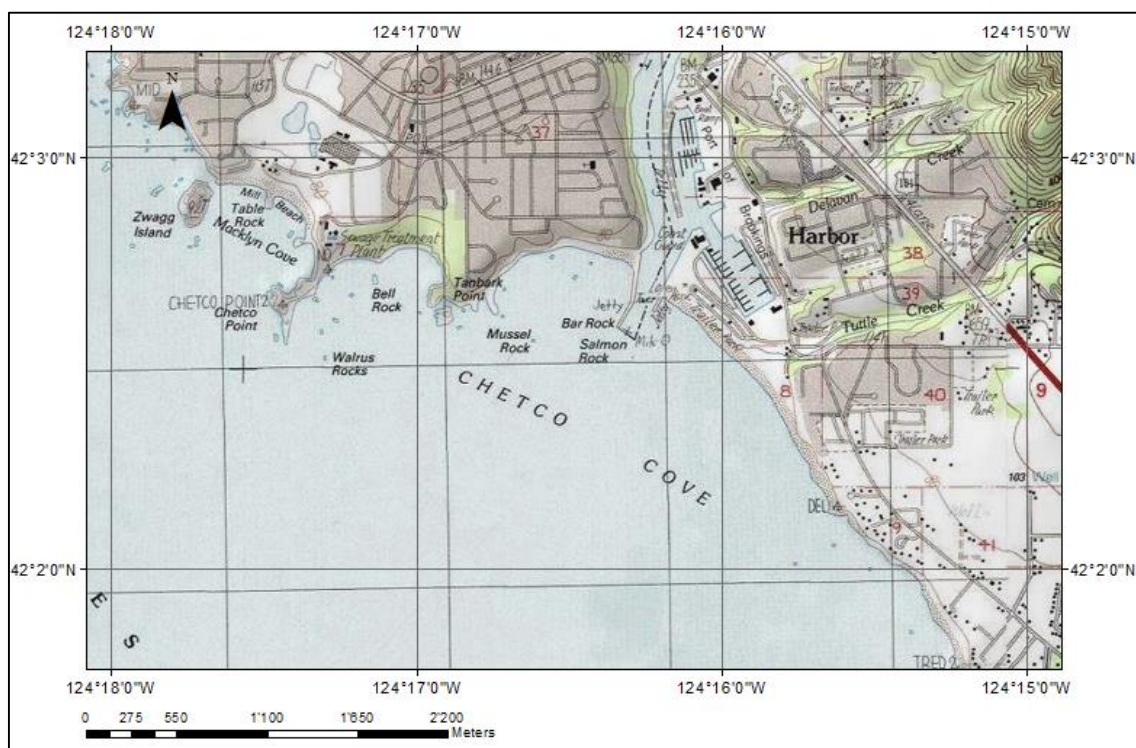


Figure 3: Topographical plan view of Chetco River Mouth showing the location and Chetco Cove

The Rogue River (Figure 5) has drainage area of approximately 13,365 km² and a mean discharge rate of about 188 m³/s. The entrance of the Rogue River provides 2 jetties and a 4 m deep channel from the ocean (Figure 4). Its estuary is .approximately 7.6



Figure 4: Rogue River Mouth plan view from a Google-Earth image. River Mouth width (W) = 285m. River orientation: 55° N.

km² during winter flows and is less during summer flows. The estuary is river-flow dominated, the mean high tide on the Rogue River is 1.5 m, and these tides extend approximately 6.4 km from the mouth to a riffle below Edson Creek.

The mean higher high water (m.h.h.l) is 2 m.

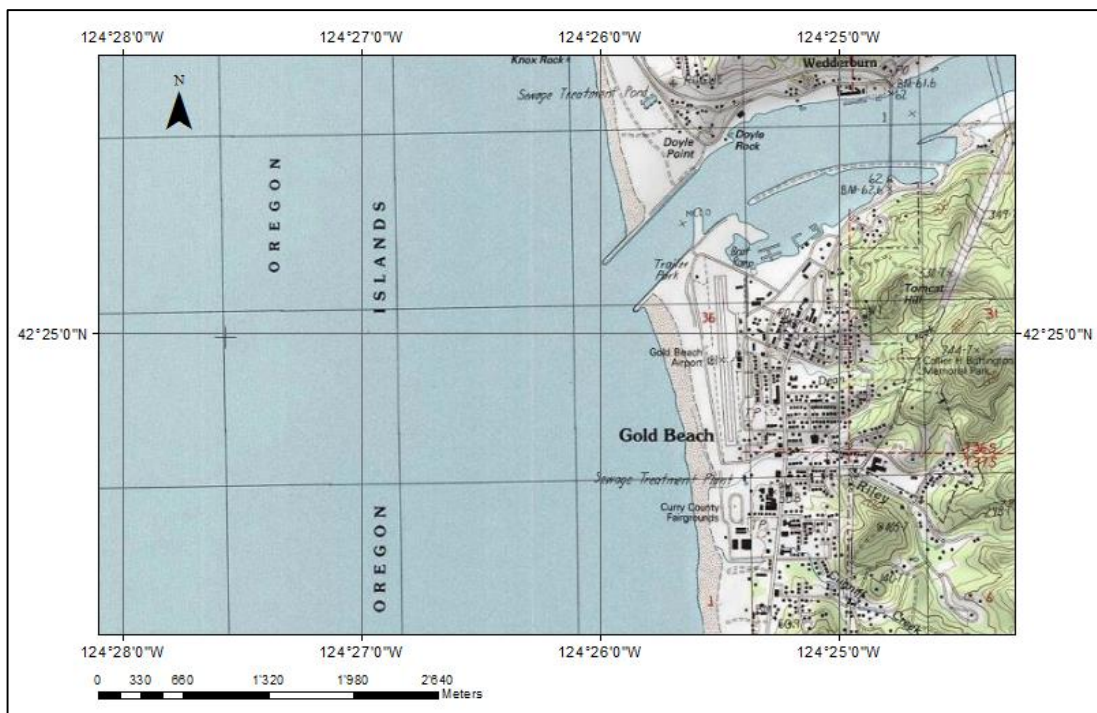
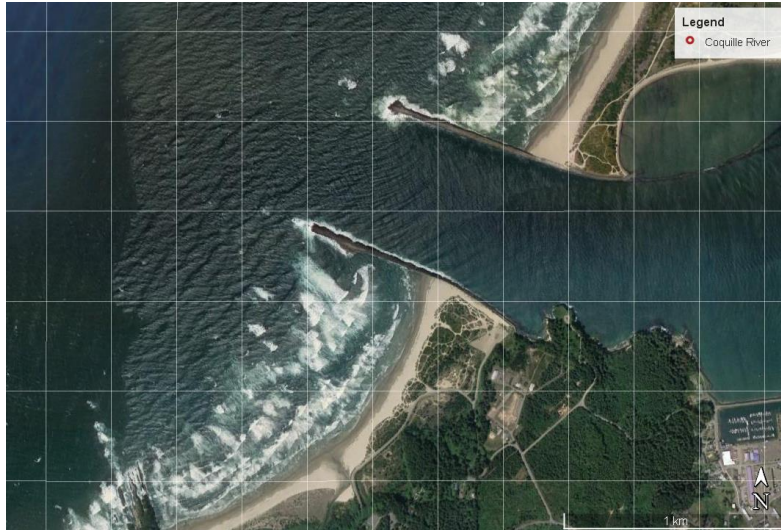


Figure 5: Topographical plan view of Rogue River Mouth showing the location and the direct discharge

The Coquille River (Figure 7) has a watershed of 2,740 km² and an average discharge rate of 128 m³/s. With three major tributaries, more water always flows out into the ocean than enters with the tide. The tidal range between mean lower low water (m.l.l.w) and mean higher high water (m.h.h.w) is 2.07 m and the extreme tidal range is about 3 m. The Coquille River Entrance is approximately 610 meters and has a depth of



4 meters (Figure 6). River flows in the Coquille reflect the seasonal distribution of precipitation and the lack of snowpack.

Figure 6: Coquille River Mouth plan view from a Google-Earth image. River Mouth width (W) = 610 m. River orientation: 115° N

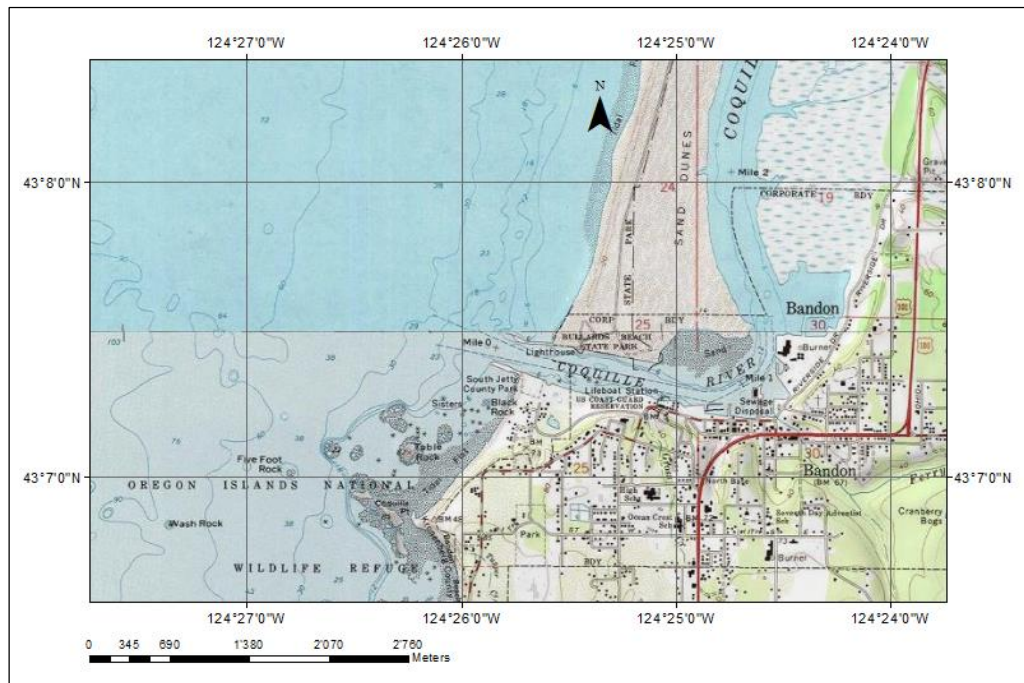


Figure 7: Topographical plan view of Coquille River Mouth showing the location and the direct discharge

The Siuslaw River is approximately 180 km long, has a drainage area of about 2,000 km² and an average discharge rate of 56 m³/s. The river mouth is inserted between



two breakwaters with an opening of 200 m (Figure 8) and an average depth of 5m. The estuary is well mixed during the summer and two-layered during the winter when high stream flows and

high tides create a two-layered system unlike the summer season where low flows and low tides can combine to shift the classification toward a mixed system (*Siuslaw River Jetty Extension, 1976*).

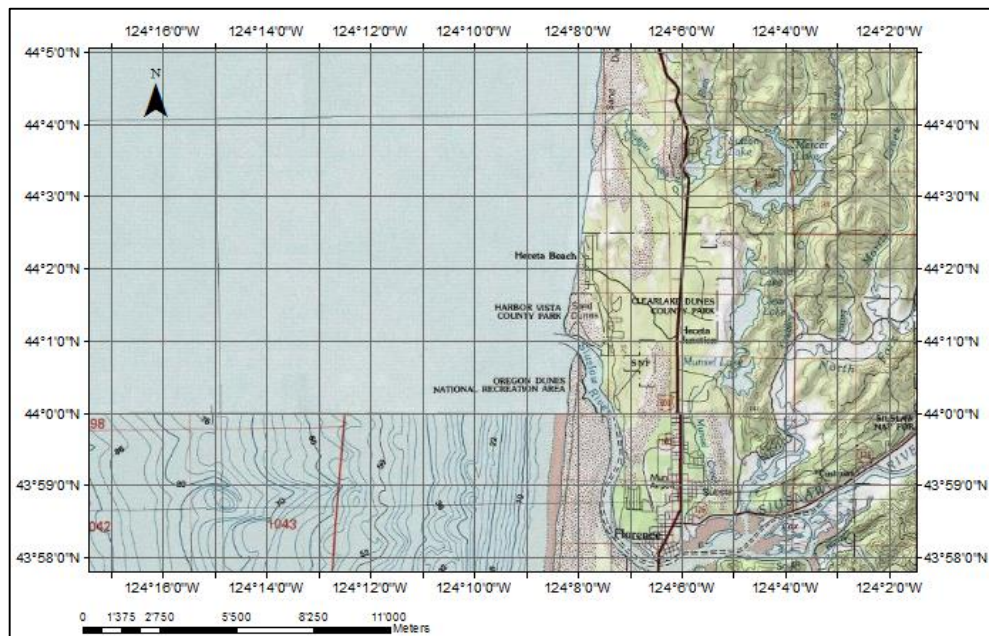


Figure 9: Topographical plan view of Siuslaw River Mouth showing the location and the direct discharge

Table 1: Monthly mean discharge rate (m³/s) for the four rivers based on the years of record at the rivers gauges (Source: USGS river flows)

Q _{mean} (m ³ /s)	Jan	Feb	Mar	Apr	May	Jun	Jul	Aug	Sept	Oct	Nov	Dec	Record Period	USGS Station
Chetco River	145	120	111	71	35	18	6	3.3	5.1	15	88	152	1969-2015	Brookings
Coquille River	90	45	38.5	26	13	5	2	1	1.25	5.3	28	50	1930-2016	South Fork
Rogue River	331	271	252	193	154	102	63	57	52	54	127	282	1960-2016	Agness
Siuslaw River	134	111	97	62	30	17.5	7.5	4.33	4.76	10	57.5	132	1968-2016	Mapleton

Table 2: Summary of the four rivers hydrological characteristics at the gauge station and the river mouth

	Chetco	Coquille	Rogue	Siuslaw
USGS Station Monitoring No	14400000	14325000	14372300	14307620
Gauge Station to river mouth (Km)	11	95	50	32
Mean Discharge (m ³ /s)	64	22	162	56
Catchment Area (Km ²)	703	438	10,202	1,523
River Length (Km)	90	58	346	180
River Mouth Depth (m)	4-5	3-4	4	4-5
River Mouth Width (m)	80	610	285	200

B. Landsat 7 ETM+ imagery

Landsat 7 Enhanced Thematic Mapper (ETM+) images were used for mapping and characterizing the thermal plumes. The instrument installed on Landsat 7 is the ETM+; a passive sensor that measures solar radiation reflected or emitted by the Earth's surface. Landsat 7 was chosen because of its relatively high spatial resolution compared to other free-satellite images and its improved data quality compared to its predecessors (e.g., Landsat-5) including on-flight radiometric and geometric calibration and an enhanced 60-m spatial resolution thermal infrared (TIR) band (Yang et al., 2003). This instrument can be effectively used for the study of spatial and temporal aspects of thermal plumes in coastal/oceanic waters (Thomas et al., 2002a). Landsat 7 has two TIR bands (band 6.1 and 6.2) which range between 10.31 and 12.36 μm representing emitted energy or radiant temperature by the target.

Table 3: Spectral and spatial resolution of Landsat 7 ETM+ bands

Landsat 7 ETM+	Band#s	Wavelength (μm)	Spatial Resolution
Blue	1	0.45-0.52	30 m
Green	2	0.52-0.60	30 m
Red	3	0.63-0.69	30 m
Near Infrared	4	0.77-0.90	30 m
Shortwave IR-1	5	1.55-1.75	30 m
Shortwave IR-2	7	2.09-2.35	30 m
ETM+ Thermal IR	6	10.40-12.50	60 (30) m
Panchromatic	8	0.52-0.90	15 m

Note that ETM+ band 6 is acquired at 60-meter resolution, but products are resampled to 30-meter pixels.

On-orbit radiometric calibration methods results indicate that the Landsat-7 ETM+ absolute radiometric calibration is stable to better than 1.5% /year in the reflective bands and 0.1% /year in the thermal band (Markham et al., 2003). The uncertainty in the calibration is estimated at <5% in the reflective and ~1% in the thermal regions (Markham et al., 2003). A 0.092 W/m²/μm/sr (0.68K at 300K) calibration offset

error was found in the TM thermal band process based on important calibration data between 1999 and 2006. This error was corrected on April 2007 for all data acquired since April 1999.

All ETM+ data were obtained as Data Level 1 (Standard Data Products) using images that are cloud-cover free around the corresponding river plume zone. Image processing was conducted using ENVI, a complete remote sensing software used to process and analyze geospatial imagery. All Landsat images georeference formats include a UTM projection (UTM_Zone_10N) and a WGS84 datum and ellipsoid.

The effective at-satellite temperature, T , was computed using

$$T = \frac{K_2}{\ln\left(1 + \frac{K_1}{L_\lambda}\right)} ; \quad (1)$$

Where T is the effective at-satellite temperature in Kelvin (K) and L_λ is the spectral radiance in $\text{W}/\text{m}^2/\mu\text{m}/\text{sr}$. The SI unit of radiance is the watt per steradian per square meter ($\text{W} \cdot \text{sr}^{-1} \cdot \text{m}^{-2}$); “ μm ” to account for the wavelength of the specters.

The retrieved at-satellite temperature from the ETM+ thermal infrared channels was found to be comparable with in situ temperature measurements taken by Germany’s National Meteorological Service, DWD (Wloczyk et al., 2006). Furthermore, the accuracy of Sea Surface Temperature (SST) estimates from Landsat data were found to be within 0.6 and 0.8 °C from the real temperature data(Thomas et al., 2002b).

C. Landsat 7 imagery and Flow data collection

Time series of Landsat ETM+ band 6.1 thermal infrared images over the period 1999-2015 were used to characterize the thermal plumes discharged at river mouth area. The images were chosen between end of September and mid-May corresponding to the period of higher flows and sharper thermal contrast. The low river discharge rate for most of these rivers during the summer months (see Table 1) and the low temperature gradient between river and ocean water temperatures constrained the use of the summer images. Table 4 shows the locations of rivers mouths, the number of images considered and the path and row of the USGS images. All the images were taken around 19:00 h local time.

Table 4: WRS coordinates of Study Rivers images (path, row), Rivers Mouths locations (Lat, Long) and the corresponding number of images.

River Name	Path	Row	Nb. Images	Latitude	Longitude
Chetco	46-47	31	56	42° 07' 25"	124° 11' 10"
Coquille	46-47	30	36	43° 07' 25"	124° 25' 48"
Rogue	46-47	31	57	42° 34' 43"	124° 04' 30"
Siuslaw	46-47	29-30	22	44° 01' 01"	124° 08' 14"

To allow for model validation, independently measured *in situ* discharge data for the study period is needed to compare with the discharge predictions from the Landsat 7 images. Those independent measurements were obtained from the USGS stations placed along the rivers courses (see Table 4), which provided high temporal resolution datasets (a measurement every 15 minutes) to monitor the flow rate before and at the time of image capture. Furthermore, to ensure that the discharge rate measured at the USGS stations corresponds well with the discharge captured by the Landsat 7 images, only images having 8 hours of steady-state flow before the image capture time were considered. Steady state was assumed when the standard deviation was less than 5% of the mean

discharge within the 8 hours just before the Landsat 7 image was captured (see Figure 10). Finally, the USGS monitoring stations were not located at the river-mouths, thus the effect of the downstream watershed was neglected considering its minimal contribution compared to the upstream flow.

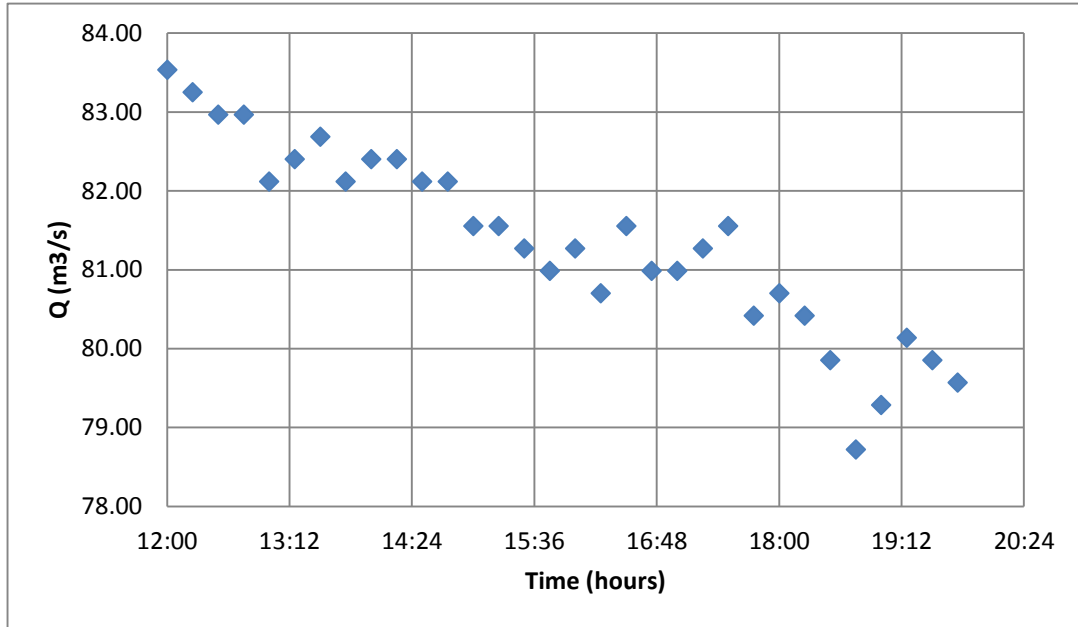


Figure 10: Hydrograph of Chetco River on 9/2/2010. The time range is from 12:00 till 20:00. The mean discharge rate is 81.37 m³/s, the standard deviation is 1.2 m³/s and the percentage of standard deviation from the mean is 1.47%.

Tables 5 and 6 summarize the total number of images available and used in the study after the images selection process based on the criteria:

- Images from September to May: Summer months (June, July and August are excluded);
- Images with free cloud cover around the studied rivers;
- Images with steady state flow with $\sigma_{\text{flow}}/Q_{\text{mean}}$ less than 5%;
- Images in which the plumes were detected by the Landsat 7 thermal sensors.

Table 5: Landsat 7 ETM+ SLC-on images (1999-2003) available based on adopted criteria for images selection

River Name	Total No of images from USGS (till 2003)	Total No of images from Sep to May	Total No of images with free cloud cover around river	Total No of images with steady state flow	Total No of images with $R_d < W$ and $h_b < D$	Total No of images with plumes detected	Total No of images used in the study
Chetco	162	119	56	36	36	26	26
Coquille	176	133	50	32	32	12	12
Rogue	162	119	62	45	45	30	30
Siuslaw	352	266	114	70	70	7	7

Table 6: Landsat 7 ETM+ SLC-Off images (2003-2015) available based on adopted criteria for images selection

River Name	Total No of images from USGS (till 2003)	Total No of images from Sep to May	Total No of images with free cloud cover around river	Total No of images with steady state flow	Total No of images with $R_d < W$ and $h_b < D$	Total No of images with plumes detected	Total No of images used in the study
Chetco	360	266	98	50	50	35	30
Coquille	550	409	135	92	92	24	24
Rogue	360	266	96	61	61	40	27
Siuslaw	901	618	219	153	153	10	10

CHAPTER III

METHODOLOGY

In this section, we describe the proposed methodology for estimating the river discharge rate from remotely sensed thermal plumes information. **Error! Reference source not found.** summarizes the steps of the adopted methodology.

In summary, the images are processed in a geospatial software (ENVI) to retrieve the different temperature areas and identify the spatial extent and shape of the thermal plume. Then, examined plume are characterized by extracting defined geometric plume characteristics (length, deviation angle). Finally, a multiple linear regression model for obtaining rivers' discharge rate is established using rivers-discharge data from the USGS stations.

Image processing includes radiometric corrections and gap-filling of Landsat ETM+ SLC-OFF images.

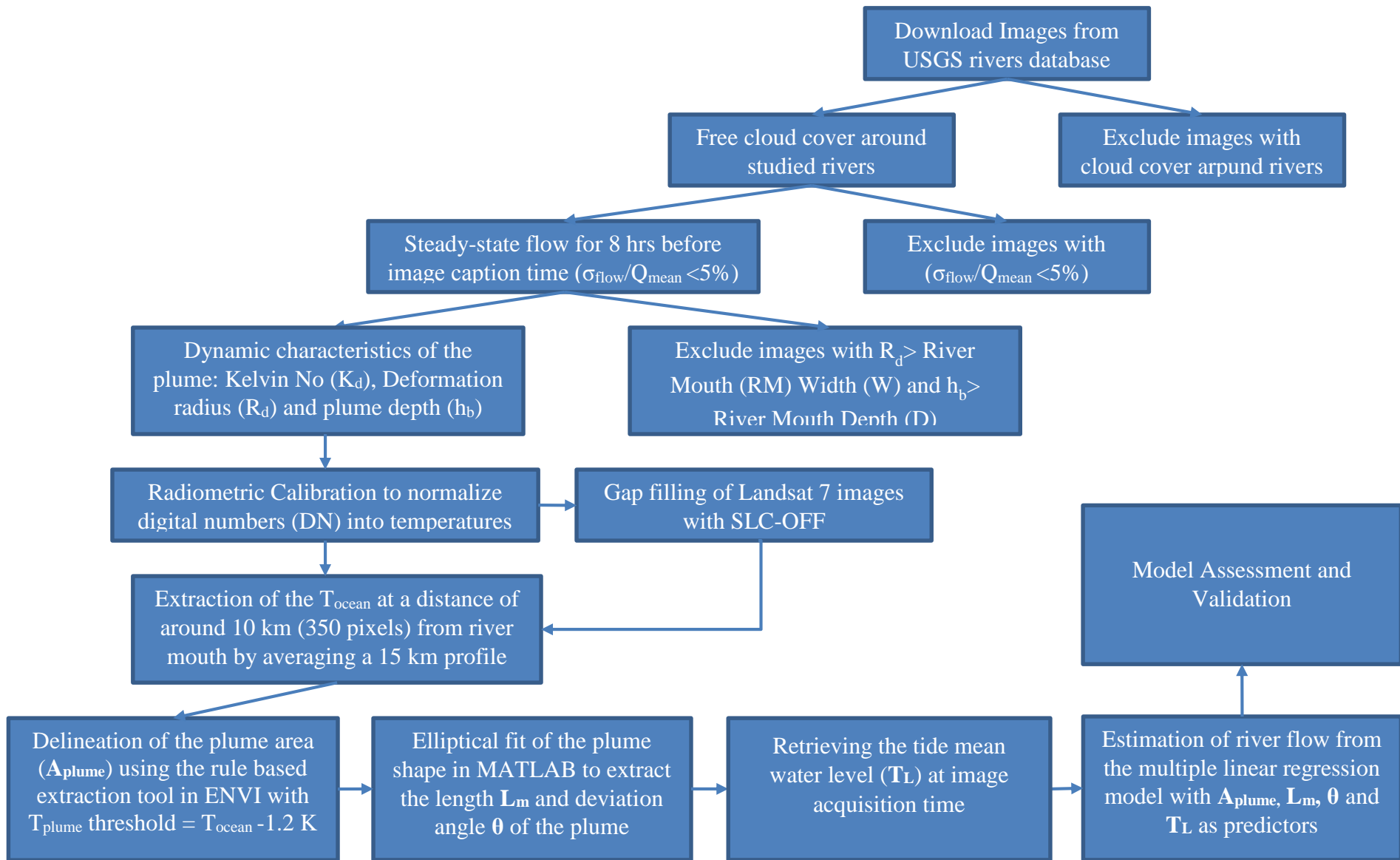


Figure 11: Summary of the proposed methodology used to estimate river flow from discharge thermal plume characteristics observed by the Landsat 7 ETM+ images

A. Image processing

1. Radiometric Correction

Buoyant river plumes and surrounding coastal waters possess very different physical and chemical properties (Cannizzaro et al., 2013). Therefore, different measurable ocean surface characteristics can be employed to distinguish buoyant plumes in coastal areas. Previous studies successfully mapped river plumes, including plumes formed by relatively small rivers, using Colored Dissolved Organic Matter (CDOM), Chlorophyll-a (Chl-a), and Total Suspended Sediments (TSS) retrieved from the satellite instruments (Birkett et al., 2002; Coynel et al., 2005). Others showed that thermal infrared characteristics of the satellites have been very effective for observing coastal plume on the shelf and in the open ocean (Thomas et al., 2002b). Here, we utilized thermal plumes since they are directly retrieved from thermal IR bands, which are easier to obtain than other characteristics.

Thermal plumes were obtained by normalizing or rectifying the intensities or digital numbers (DN) of different images into brightness temperatures using the standard built-in radiometric calibration tool from ENVI (Lo & Yang, 1998). This method uses the calibration constants K1 and K2 to calculate the relative brightness temperature from the calibrated spectral radiance parameter L_{λ} .

In this study, no further atmospheric correction (Barsi et al. (2003)) was applied beyond the radiometric correction due to data limitations about the emissivity of the target in order to determine L_T (L_T is the radiance of a blackbody target of kinetic temperature T).

2. Landsat ETM+ SLC-OFF gap filling

After radiometric correction, the gaps of Landsat ETM+ SLC-OFF images were treated using the Landsat Gapfill tool for ETM SLC-off data developed by USGS and

incorporated in ENVI (see Figure 12). We performed the single file gap-fill using a triangulation method. The tool assumes that the same-class neighboring pixels around the un-scanned pixels have similar spectral characteristics, especially for homogeneous landscapes (example plume area), and that these neighboring and un-scanned pixels show similar patterns of spectral differences (J. Chen, 2011).

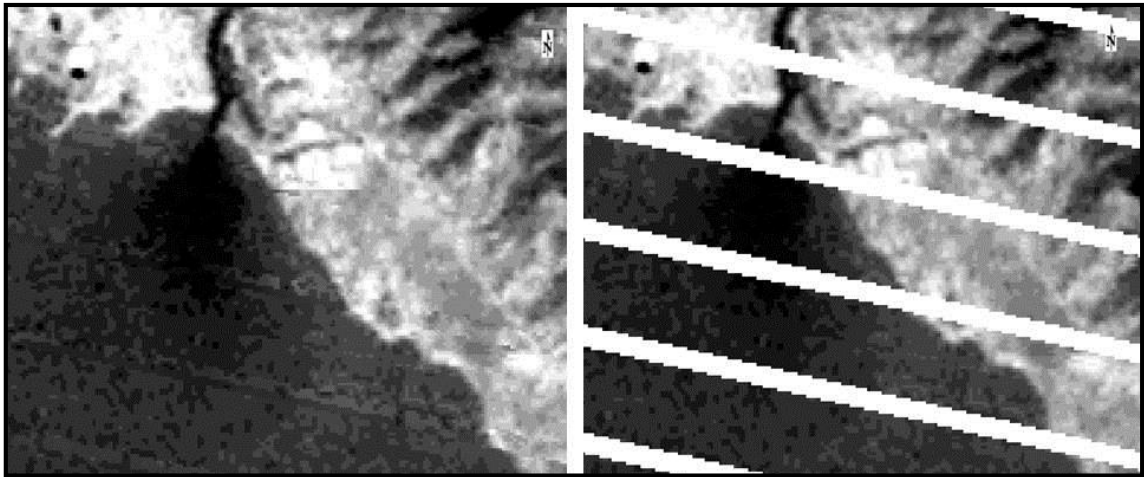


Figure 12: Gap filling of Landsat 7 SLC-off scenes using ENVI toolbox feature

B. Dynamical characterization of the plume

Discharged river flows into ocean were verified against some readily measured criteria (e.g. (Richard W Garvine, 1995; Yankovsky & Chapman, 1997) to classify their dynamics and improve our comprehension of their corresponding plumes behavior. The conducted verification parameters are the plume scale, tidal effect and plume's shallowness.

Richard W Garvine (1995) classified buoyant plumes as “small-scale” or “large-scale” using the bulk Kelvin number, K , to assess the relative importance of rotational and inertial processes. Large-scale plumes leave their source and turn downshelf, creating a geostrophically balanced coastal current that transports buoyant water downshelf of the mouth. Small-scale plumes are governed by inertial dynamics and tend to form freshwater bulges that radiate in all directions from the source.

The bulk Kelvin number is expressed as:

$$K = \frac{R_p}{R_D}; \quad (2)$$

However, the dynamics governing the flow vary based on the location within the plume.

At the river mouth, the Kelvin number is defined as (Yankovsky & Chapman, 1997):

$$K_m = \frac{W}{R_D}; \quad (3)$$

where W is the mouth width used as the characteristic length scale and,

$$R_D = \sqrt[4]{\frac{2*Q_R*g'}{f}}; \quad (4)$$

With f is the Coriolis parameter, $g' = g (\rho_{amb} - \rho_o)/\rho_o$ where g is the gravitational acceleration, ρ_{amb} the ambient ocean density, and ρ_o the density of the incoming freshwater and Q_R the discharge rate of the river. Large Kelvin numbers ($K \gg 1$) are indicative of “large-scale” plumes, and small Kelvin numbers ($K \ll 1$) indicate “small-scale” plumes. The Kelvin number is a geometric parameter that reflects length scales of the plume.

After that, plumes were verified against the hypothesis of being surface-advected plume by calculating the empirical predicted plume’s depth using only discharge parameters as expressed in equation 5 (Yankovsky & Chapman, 1997) and comparing it to the mean depth of the river mouth area as indicated in section A:

$$h_b = \sqrt{\frac{2*f*Q_{USGS}}{g'}}; \quad (5)$$

A value of h_b that is less than the mean depth of the region indicated a “surface-advected” plume and a value of h_b that is greater than the mean depth of the region indicates a “bottom-advected” plume.

Finally, tides can also change the plume characteristics (shape, thickness and location). The ratio of the cross-sectional averaged freshwater velocity to the average tidal current is used to classify this influence (Tilburg et al., 2011).

$$P = \frac{Q_{R*}W}{h_o u_t}; \quad (6)$$

Where h_o is the average river-mouth depth and u_t is the mean tidal speed. Large values of the tidal index ($P>1$) indicate a buoyancy governed flow, while small values of the tidal index ($P<1$) indicate tidally driven flow.

Results of plumes dynamical characterization for each river are listed in Appendix VI.

C. Delineation of the plume's area

Once the corrected brightness temperatures were obtained, the next step was to delineate and extract the plume areas using the rule based feature extraction wizard in ENVI. The dynamics of any buoyant plume can be generalized by dividing the plume into two areas: the near field area, and the far field area (Jirka et al., 1981).

The near field is defined as the region whose characteristics are dominated by the initial discharge conditions. These include the discharge velocity (momentum), and the discharge temperature, salinity(Jirka et al., 1981). In this area, the momentum dominates over the buoyancy. This field area acts as a transition between the river discharge and the ocean and constitutes the initial conditions of the far-field plume. Thus, understanding the characteristics of the near-field plume will allow us to relate the discharged flow to the larger scale coastal environment. On the other hand, the far field is defined as that region of the plume that is less influenced by the initial characteristics of the discharge and more dominated by the natural processes of water movement like currents and turbidity.

Many studies and simulations coupled the near and far field areas to assess the behavior of the discharged plume (Cole & Hetland, 2016; D.R. Johnson et al., 2003; Kaufman & Adams, 1981). However, Cole and Hetland (2016) showed that some of the rivers large scales non-constricting rivers, which river mouths width (**W**) are much wider than the produced deformation radius **R_d** of the plume, the near-field of the plume cannot be detected alone. In this case, the plume's area is considered as one single plume entity with no distinction between near field and far field regions.

In this study, all four rivers have river mouths width wider than the calculated deformation radius of the flows. Therefore, we will consider the plume's area shown by the Landsat images as one single plume entity (refer to VI for deformation radius **R_d** calculations).

With respect to plume boundaries, plume borderline can be defined by a threshold value for the temperature isoline (Walker et al., 2005). The threshold value defining the plume borderline is dependent on the river and ocean average temperatures that vary for every image. Depending on those averages, the temperature of the plume changes increasingly or decreasingly towards the ambient ocean water temperature (F. Chen & MacDonald, 2006).

The radiometric resolution of a satellite specifies how well the difference in surface water brightness temperature in an image can be perceived; this is measured through the number of grey value levels. The number of bits defines the maximum number of values. For Landsat 7 ETM+, the 8-bit representation has 256 grey values. Additionally, the useful temperature range (K) for low (L) and high (H) gain settings for Landsat 7 ETM+ are defined as follow (Barsi et al., 2003):

For low gain settings: $T_{\min} = 130 \text{ K}$, $T_{\max} = 350 \text{ K}$.

For high gain settings: $T_{\min} = 240 \text{ K}$, $T_{\max} = 320 \text{ K}$.

Therefore, each grey value represents 0.86 K in the low gain settings and 0.31 for the high gain settings, thus around 0.6 K for their combination. Based on this, the differentiation between the plume area and the ocean waters is set to be two grey values, i.e. 1.2 K and thus the outer area of the plume shall be excluded (Figure 13). Thus, we defined the threshold value based on the retrieved ocean ambient water temperature.

$$T_{\text{Threshold}} = T_{\text{Ocean}} - 1.2 \text{ degrees};$$

Table 7 shows the followed procedure for the delineation of the plume area:

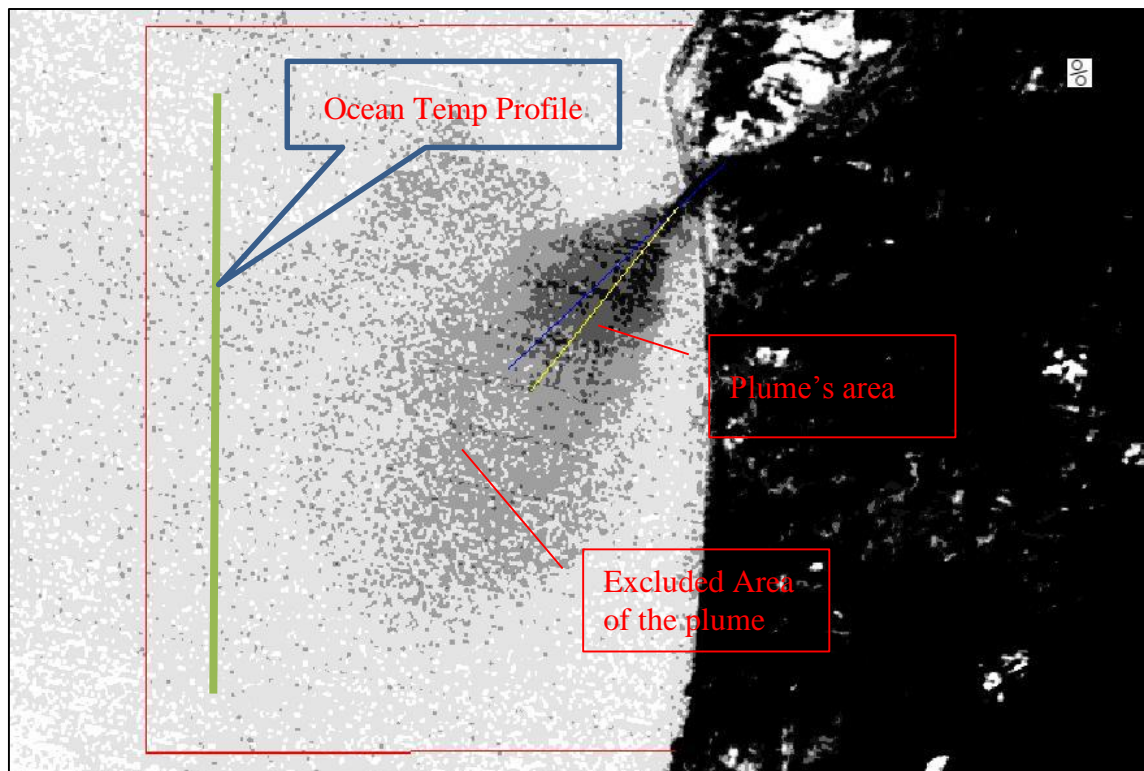


Figure 13: Landsat 7 ETM+ image from Rogue River (17/3/2003) showing the plume's area and the excluded part of the plume and the defined boundary limit of the river.

Table 7 shows the followed procedure for the delineation of the plume area:

Table 7: Shown the description of the parameters needed for the river plume’s area definition

Steps	Parameter	Description of extracted parameters
1	T_{ocean}	Ocean surface water temperature “ T_{ocean} ” was retrieved from Landsat images at a distance of around 10 kilometers (350 pixels) from the river mouth, to avoid the proximity of the plume, by averaging the values of a rectangular area of 5 pixels by 100 pixels parallel to the coastline (see Figure 13).
2	$T_{\text{excluded-area}}$	The excluded area is defined as the plume’s area with a temperature difference of +/- 0.6 K from the T_{ocean}
3	A_{plume}	Delineation of the plume area using the rule-based feature extraction tool in ENVI by defining a spectral temperature range between the minimum temperature found at the river mouth and $T_{\text{threshold}}$ as defined above.

The rule-based feature extraction tool in ENVI was utilized for plume area extraction. The tool uses an object-based approach to classify imagery, where a segment is a group of pixels with similar spectral, spatial and/or textures characteristics. Several setting-combinations were tested to ultimately choose the best representation of the observed plume. The use of segmentation and merging scales with the levels 0 and 10, respectively were found to represent the most accurate shape of the thermal plume (see Figure 14). A spectral rule base, herein temperature, was used to define each class (area) constituting a defined temperature interval. In rule classification, similar pixel clusters are grouped into classes within a segmented image. Those groups are used to partition the image into objects. The process permitted plume tracing based on its spectral/temperature characteristic and was repeated for every image (see Figure 15). Assessment of the “rule-

based feature” extraction method by ENVI was conducted and is summarized in the following section.

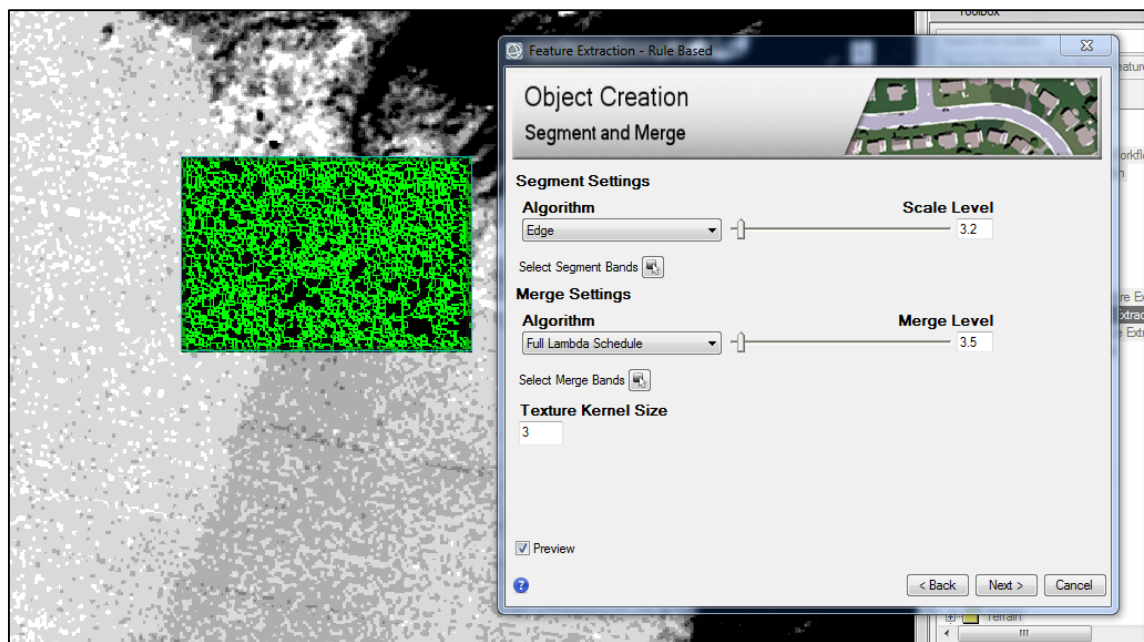


Figure 14: Example of the rule-based feature extraction tool in ENVI to define the scale and merge levels required for the segmentation of the region of interest around the plume’s area.

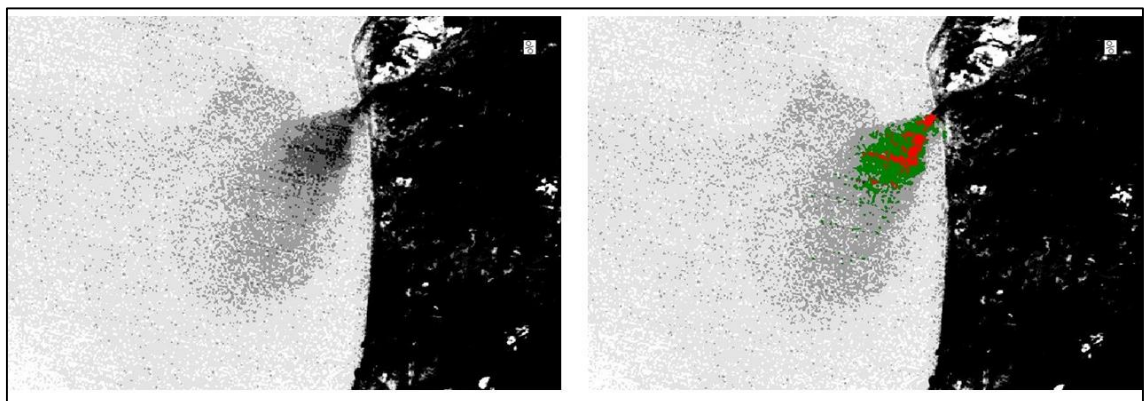


Figure 15: Landsat 7 ETM+ image of Rogue River (23/02/2002) showing the extracted plume areas using the rule-based feature extraction tool in ENVI. Plume area is the combination of both areas marked in green and red.

D. Evaluation method of the plume’s area ENVI extraction method

- 1) The performance of the plume classification model, using ENVI’s rule based feature extraction tool, was assessed using the contingency tables by comparing the tool’s classification to the true classification as obtained from manual digitization. Classification model outputs were aggregated in contingency tables

and analyzed by calculating skill scores. The contingency table, also known as the error matrix, is a table format allowing visualization of the performance of a classifier by reporting the following four metrics (True Positive (**TP**): It reports, in number of pixels, the intersection area between both extraction methods (“ENVI” and “Manual” methods).

- 2) False Positive (**FP**): It represents, in number of pixels, the part of the ENVI plume that did not overlap an area of the Manual plume.
- 3) False Negative (**FN**): It represents, in number of pixels, the part of the Manual plume that was missed by the ENVI plume.
- 4) True Negative (**TN**): It represents, in number of pixels, the area outside Manual and ENVI plume regions.

Table 8).

- 5) True Positive (**TP**): It reports, in number of pixels, the intersection area between both extraction methods (“ENVI” and “Manual” methods).
- 6) False Positive (**FP**): It represents, in number of pixels, the part of the ENVI plume that did not overlap an area of the Manual plume.
- 7) False Negative (**FN**): It represents, in number of pixels, the part of the Manual plume that was missed by the ENVI plume.
- 8) True Negative (**TN**): It represents, in number of pixels, the area outside Manual and ENVI plume regions.

Table 8: Example of a contingency table showing the nomenclature of the different relations

Tested Method “ENVI”	Reference Method “Manual”			
		Positive	Negative	Total
Positive		TP	FP	

	Negative	FN	TN	
	Total			

In addition, statistical indicators like bias score (BIAS), true positive rate (TPR), F score (F), and Heidke Skill score (HSS) were considered and are briefly described below.

Bias Score (BIAS) is the ratio of the number of yes from tested "ENVI" method divided by the number of yes from reference "Manual" method. It ranges from 0 to 1 with a perfect score of 1. If Bias >1, tested method tend to overestimate compared to the reference and vice versa if Bias <1.

$$\mathbf{BIAS} = \frac{TP+FP}{TP+FN}; \quad (7)$$

True Positive Rate (TPR) measures the proportion of true positive values over positive values indicated by the reference method. It ranges from 0 to 1 with a perfect score of 1.

$$\mathbf{TPR} = \frac{TP}{TP+FN}; \quad (8)$$

F score is an accuracy measurement. It can be interpreted as a weighted average of the precision and TPR. The precision is the positive predictive value (**PPV= TP/ (TP+FP)**). The F score reaches its best value at 1 and worst at 0.

$$\mathbf{F} = \frac{2*TP}{2*TP+FP+FN}; \quad (9)$$

Heidke Skill Score (HSS) is a measure of skill in predications. It is defined as follows:

$$\mathbf{HSS} = \frac{NC - E}{T - E}; \quad (10)$$

where NC equals the number of times the "ENVI" and the "Manual" methods match, T equals the total number of observations, and E equals the number of observations by

“ENVI” to verify based on chance. The range of the HSS is $-\infty$ to 1. Negative values indicate that the random classification is better, 0 means no skill, and a perfect classification obtains a HSS of 1.

In other terms HSS can be expressed as follows,

$$\text{HSS} = \frac{2 * (TP + TN)}{[(TP + FN) * (FN + TN) + (TP + FP) * (FP + TN)]}, \quad (11)$$

Evaluation results and interpretation for the performance of the method applied for the four rivers are shown in the Results section.

E. Determining the plume geometric characteristics

Following plume area extraction, two additional plume geometric characteristics were determined: the length scale L_m associated with the inflow and the angle θ between L_m and the river centerline (see Figure 16). The plume length, as defined by (Jones et al., 2007), was used for flow classification and to describe flow stability and boundary interaction. It describes the relative importance of discharge volume flux, momentum flux and the distance over which these dynamic quantities control the flow. Here the L_m length describes the distance of the plume area from the river mouth center to the plume boundary. R.W. Garvine (1995) showed that this distance is related to a ratio of the momentum and buoyancy fluxes at the source.

At first, the plume length L_m of each plume was measured manually from the center point at the end of the river mouth until the mid-point of the plume’s borderline. The results induced using this method are summarized in the results section in Tables 15 & 16.

For a better representation of this length in an automated method, the major axis length of a generated ellipse in MATLAB fitting the perimeter of the plume is considered (see Appendix VIII for the details of the fitting process). This representation shall take the

place of the manual measurement of the plume length L_m by the user and thus avoid his influence on the measurements.

The procedure consisted of fitting an elliptical form (see Figure 17) around the irregular shape of the plume delineated in ENVI based on the principal component analysis (PCA). The shape of the plume is imported into MATLAB and converted into a binary image. Afterwards, the best fitting ellipse representing the area of the plume shape and accounting for the most number of pixels is calculated. The major axis length is then extracted and it represents the plume length L_m . The accuracy rate and TPR score based on confusion matrix of the overlap between the plume and the ellipse area are calculated for each image (see Figure 18).

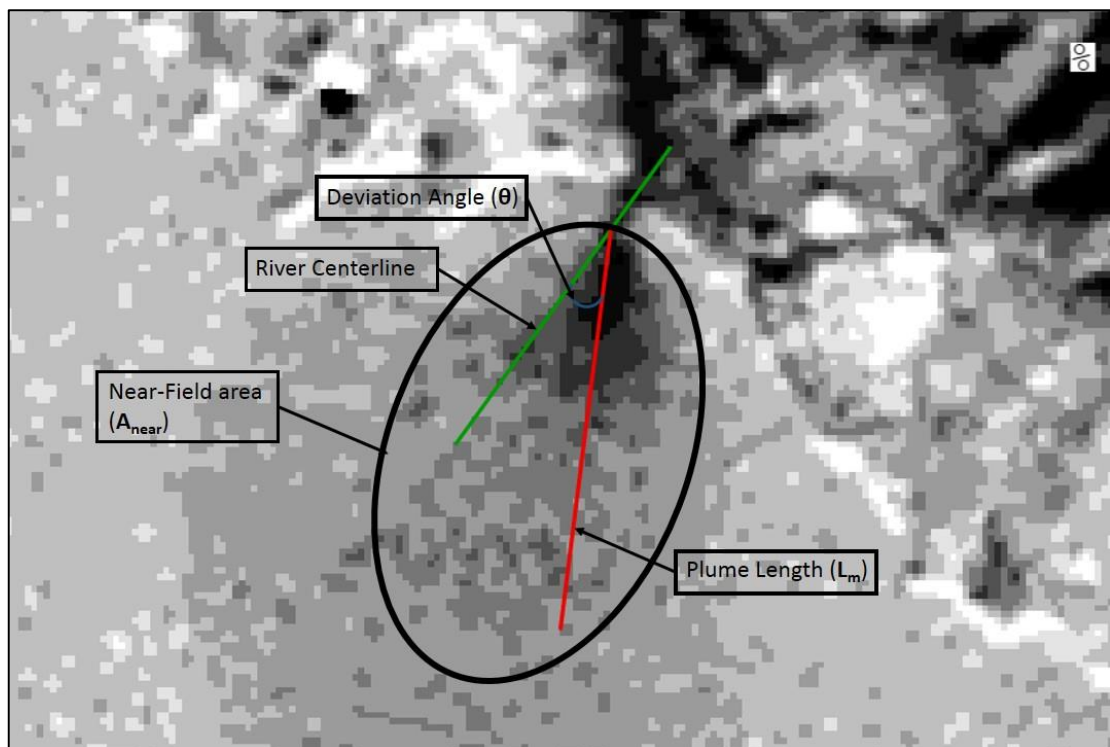


Figure 16: Landsat 7 ETM+ image of Chetco River (19/1/2001) showing the geometric characteristics of the plume (Plume Length L_m in red till the end of the plume extent, River Centerline in green, and Deviation angle (θ) between the two lines.

The angle “ θ ” between the length scale L_m and the river centerline represents the effect of the ambient current, the wind driven force and the rotational forces on the plume. The

lack of precise wind and current data at local scale near the river area prevent us from using the available shoreline measurements of these parameters in our analysis. Instead, the angle θ considered as the geometric parameter is used to characterize the influence of these factors. Walker et al. (2005) showed a relationship between plume's orientation and wind direction exhibiting a strong influence on the size of Mississippi river plume.

The measurement of the deviation angle " θ " was done manually for each image between the fixed segment representing the river centerline and the plume length measured by the user. An automated method was then introduced using MATLAB; the river centerline was imported from ENVI to MATLAB and the angle between this centerline and the major axis of the ellipse was calculated (see Figure 17).

The calculated angles and majors axes lengths were then used to estimate the rivers flows.

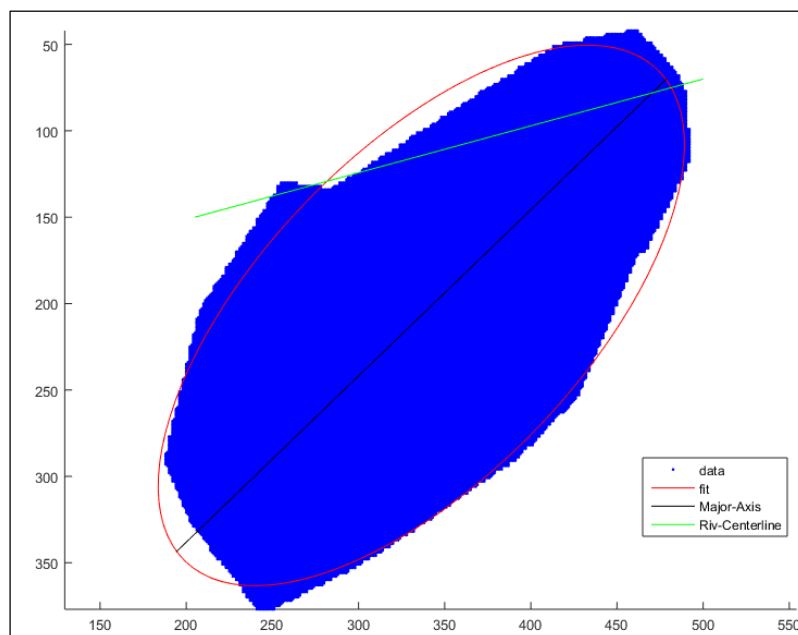


Figure 17: Plume shape of Rogue River (29/1/2000) showing in blue the extracted plume from ENVI, in red the ellipse fitting the plume, in black the major axis length representing the plume length L_m and in green the river centerline.

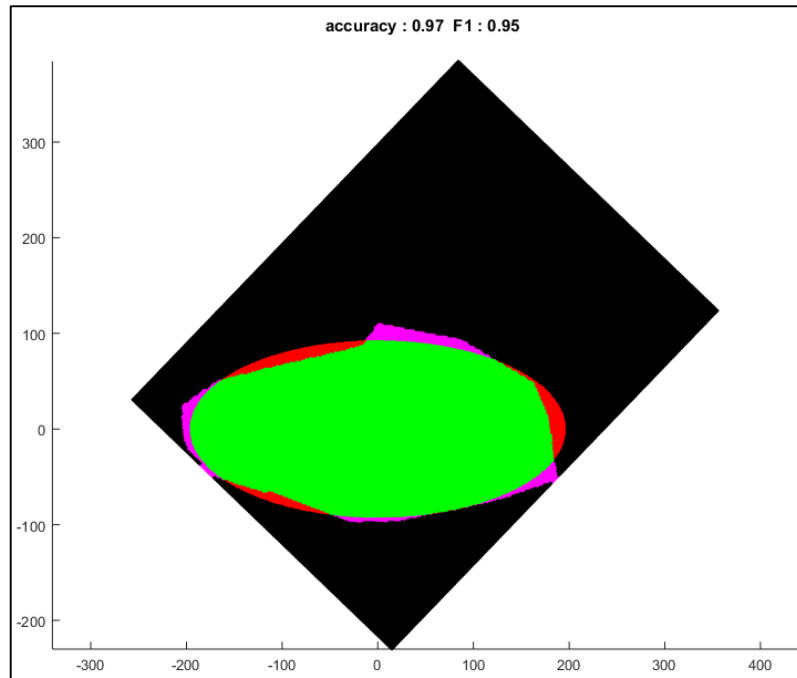


Figure 18: Showing the overlap between the plume and the generated fit ellipse the plume. The assessment performance scores: F1=0.95; Accuracy: 0.97.

Finally, the corresponding tide mean water level for each image at acquisition time is retrieved from National Oceanographic Atmospheric Administration (NOAA). Effects of tides on the plume shape and the freshwater transported is partially considered by correlating the discharged flow to the tide mean water level T_L . In their study, M. Li and Z. Rong (2012) showed that the freshwater transported by the coastal current increased with tides, indicating that the tidal currents force the plume water to move in their direction. Yankovsky and Chapman (1997) assessed the contribution of the tides levels in the fate of the buoyant coastal discharges.

F. River discharge linear model

To predict river discharge, the following multiple linear regression model with four predictors was used:

$$Q = \alpha * A_{plume} + \beta * Lm + \gamma * \theta + \delta * T_L; \quad (12)$$

Where α , β , γ and δ are the partial regression coefficients,

L_m is the length scale of the plume area expressed in number of pixels, A_{plume} is the plume area expressed in number of pixels, θ is the angle between L_m and the river centerline at the river mouth expressed in degrees, and T_L is the tide mean water level (m).

The multiple regression analysis is used to statistically derive a general equation that uses the four parameters (A_{plume} , θ , L_m , and T_L) to estimate mouth discharge in rivers. The partial regression coefficients are calculated by minimizing the mean squared error (MSE) between the measured (USGS) and estimated discharge rates.

We evaluated the multicollinearity for the predictors for each multiple regression model.

A simple approach to identify collinearity among explanatory variables is the use of variance inflation factors (VIF). VIF calculations are straightforward and easily comprehensible: the higher the value, the higher the collinearity. A VIF quantifies how much the variance is inflated. A VIF for a single explanatory variable is obtained using the R^2 value of the regression of that variable against all other explanatory variables:

$$\text{VIF}_j = \frac{1}{1 - R_j^2}; \quad (13)$$

The multi-collinearity was checked for each independent variable in function of the other variables. If VIF is more than 10, multicollinearity is strong. The VIF-scores showed that there is no collinearity between the explanatory predictors. Appendix A shows the results of the multicollinearity diagnostic tests for each river.

Different quantitative statistics were considered to assess the multiple linear regression model and are divided into three major categories: standard regression, dimensionless, and error index. In addition, diagnostic plots and “4-fold” cross-validation assessment were conducted. Standard regression statistics determine the strength of the linear relationship between simulated and measured data. Dimensionless techniques provide a

relative model evaluation assessment, and error indices quantify the deviation in the units of the data. These evaluation statistics are: The Nash-Sutcliffe (NSE), the Percent bias (PBIAS) and the RMSE-observations standard deviation ratio (RSR).

PBIAS measures the average tendency of the simulated constituent values to be larger or smaller than the measured data.

The optimal value of PBIAS is 0, with low-magnitude values indicating accurate model simulation. Positive values indicate model underestimation bias, and negative values indicate model overestimation bias. PBIAS is calculated with Eq. 14 and expressed as a percentage:

$$PBIAS = \frac{\sum_{i=1}^n (Q_i^{obs} - Q_i^{sim}) * 100}{\sum_{i=1}^n Q_i^{obs}}; \quad (14)$$

Where Q_i^{obs} is the observed discharge at time i , Q_i^{sim} is the simulated discharge at time i .

Root Mean Square Error (RMSE) is one of several error indices used in model evaluation. This index is valuable because it indicate error of the constituent of interest, which helps in analysis of the results. A standardized version of the RMSE was selected too. This model evaluation statistic is named **RMSE-observations standard deviation ratio (RSR)**. RSR is calculated as the ratio of the RMSE and standard deviation of measured data, as shown in Eq. 15:

$$RSR = \frac{\sqrt{\sum_{i=1}^n (Q_i^{obs} - Q_i^{sim})^2}}{\sqrt{\sum_{i=1}^n (Q_i^{obs} - Q^{mean})^2}}; \quad (15)$$

Q^{mean} is the mean of the observed discharges. RSR varies from the optimal value of 0 to a large positive value. The lower RSR is the better the model simulation performance.

The **Nash Sutcliffe Efficiency (NSE)** coefficient (Eq. 16) which can be viewed as an error variance normalized by the mean discharge rate of the river is used to assess the predictive power of the model. The NSE coefficient is calculated as follow:

$$NSE = 1 - \frac{\sum_{i=1}^n (Q_i^{obs} - Q_i^{sim})^2}{\sum_{i=1}^n (Q_i^{obs} - Q^{mean})^2}, \quad (16)$$

Note that a NSE value of one means the modeled and the observations are identical, while a NSE value of zero means the modeled is no better than forecasting the average discharge rate (Q^{mean}). It considers the entire range but does not provide specific information on how well peaks or low flows are predicted, for which other metrics are more appropriate.

CHAPTER IV

RESULTS AND OBSERVATIONS

A. Assessment of the “rule-based feature” extraction method- ENVI

As described in Section 0D in CHAPTER II, the performance of the “rule-based feature“ extraction method from ENVI is compared to the “Manual” extraction of the plumes by establishing contingency tables of the outputs and calculating the corresponding skill scores.

In order to dress out these tables, a boundary limit of the study area was chosen for each river. Study areas, expressed in number of pixels, are respectively 5000, 7000, 10000 and 10000 respectively for Chetco, Coquille, Rogue and Siuslaw Rivers. Table 9 below is an example of the contingency table applied to a plume area extracted manually and by ENVI method from Coquille River.

Table 9: Contingency table of plume area classification between Manual and ENVI definitions from Coquille River image dated in 19/12/1999.

n= 7000	ENVI Definition: YES	ENVI Definition: NO	TOTAL
Manual Definition: YES	454 (TP)	24 (FN)	478
Manual Definition: NO	9 (FP)	6513 (TN)	6522
TOTAL	463	6537	

Consequently, for each image, i.e. for each plume’s area, of the four rivers a contingency table was dressed out. The average, minimum, maximum and standard deviation values of the skill scores for each river was calculated and summarized in below Table 10.

Table 10: Summary of the contingency tables skill scores for the four rivers.

Rivers		TPR	F	BIAS	HSS
Coquille	Average	0.905	0.904	1.003	0.900
	Minimum	0.835	0.825	0.935	0.824
	Maximum	0.945	0.942	1.172	0.940
	Std Dev	0.03	0.02	0.05	0.02
Chetco	Average	0.924	0.923	1.003	0.914
	Minimum	0.795	0.827	0.894	0.820
	Maximum	0.969	0.966	1.073	0.961
	Std Dev	0.039	0.034	0.040	0.034
Rogue	Average	0.894	0.894	1.000	0.892
	Minimum	0.744	0.795	0.872	0.794
	Maximum	0.964	0.963	1.156	0.958
	Std Dev	0.052	0.049	0.062	0.047
Siuslaw	Average	0.906	0.901	1.012	0.896
	Minimum	0.855	0.809	0.939	0.807
	Maximum	0.962	0.956	1.113	0.950
	Std Dev	0.027	0.030	0.050	0.030

From Table 10, we can see clearly based on the BIAS values that the “ENVI” extraction method is interchangeably underestimating or overestimating the manual extracted area with an average bias value of 1.013. This indicates no bias in the “ENVI” extraction method. On the other hand, the average HSS high values, approximately 0.9, with a minimum value of 0.79 for all the rivers indicate good performance of the adopted “ENVI” extraction method over the “Manual” method.

The “ENVI” extraction method automates, standardizes and facilitates the extraction method of the plume’s area.

Contingency tables and skill scores carried out for all images of the four rivers are listed in Appendix VII.

B. Estimation of discharge rates of the rivers

The multiple linear regression model is fitted for each river with $Q_{\text{estimated}}$ as the response and the plume area (A_{plume}), the length scale (L_m), the deviation angle (θ) and tides mean level (T_L) as the predictors. Two linear models were built for each river using L_m and θ manually measured for the first model and defined in MATLAB for the second model. Results of the manual method are summarized in Table 17. The description and analysis of the results, hereafter, are detailed for the second method.

Tables 11, 12, 13 and 14 show the analyses results of these models for each river:

Because not all the parameters are significant in the initial model, a model selection based on the Akaike information criterion (AIC) is applied. The multiple R^2 , adjusted R^2 , the p-value and the final model of each river are shown in below Table 15 and 16.

Table 11: Summary of the initial/final multiple linear regression models of Chetco River

Initial	Estimate	Std. Error	t value	p value
(Intercept)	-7.612	16.129	-0.590	0.680
Aplume	0.047	0.009	4.140	0.001
Lm	0.062	0.018	3.840	0.000
Angle	-0.675	0.579	-2.456	0.145
Tides	-1.497	7.610	-0.300	0.892
Final	Estimate	Std. Error	t value	p value
(Intercept)	-6.156	14.077	-0.670	0.680
Aplume	0.135	0.010	3.570	0.001
Lm	0.075	0.020	3.820	0.000

R^2 alone can be misleading when you assess the goodness-of-fit for linear regression analysis. The adjusted R^2 compares the explanatory power of regression models that contain different number of predictors. It is a modified version of R^2 that has been adjusted for the number of predictors in the model.

Table 12: Summary of the initial/final multiple linear regression models of Coquille River

Initial	Estimate	Std. Error	t value	p value
(Intercept)	-2.149	13.975	-0.350	0.823
Aplume	0.067	0.025	3.672	0.001
Lm	0.063	0.097	1.677	0.062
Angle	-0.358	0.126	-1.125	0.324
Tides	-7.147	3.792	-2.300	0.038
Final	Estimate	Std. Error	t value	p value
(Intercept)	-4.347	10.903	-0.430	0.670
Aplume	0.056	0.014	3.420	0.002
Lm	0.281	0.015	2.060	0.048
Tides	-7.666	3.795	-2.440	0.020

Table 13: Summary of the initial/final multiple linear regression models of Rogue River

Initial	Estimate	Std. Error	t value	P value
(Intercept)	40.504	30.745	1.140	0.2063
Anear	0.061	0.054	3.300	0.0014
Lm	0.681	0.051	5.654	7.00E-07
Angle	-0.4353	0.992	-0.45	0.6562
Tides	40.314	30.147	1.222	0.2063
Final	Estimate	Std. Error	t value	p value
(Intercept)	37.671	12.183	3.560	43.353
Aplume	0.048	0.015	3.510	0.053
Lm	0.487	0.069	7.060	0.487

Table 14: Summary of the initial/final multiple linear regression models of Siuslaw River

Initial	Estimate	Std. Error	t value	p value
(Intercept)	-6.740	17.238	-0.39	0.457
Anear	0.101	0.033	3.03	0.010
Lm	0.032	0.010	3.10	0.011
Angle	0.024	0.347	0.07	0.745
Tides	5.627	6.995	0.80	0.436
Final	Estimate	Std. Error	t value	p value
(Intercept)	1.213	11.130	0.110	0.813
Aplume	0.171	0.032	3.620	0.001
Lm	0.024	0.010	3.930	0.007

Table 15: Final multiple linear regression models statistics of the four rivers based on the MATLAB automated method

River Name	R2	Adj R2	p-value	Final Model
Chetco	0.63	0.61	3.67*10-8	Qest ~ Aplume + Lm
Coquille	0.57	0.54	1.02*10-9	Qest ~ Aplume + Lm + Tides
Rogue	0.57	0.55	2.20*10-9	Qest ~ Aplume + Lm
Siuslaw	0.61	0.57	1.74*10-4	Qest ~ Aplume + Lm

Table 16: Final models equations of the four rivers using the significant parameters of each river

River Name	Final Model Equation
Chetco	$Q_{est} = 0.14 * A_{plume} + 0.08 * L_m$
Coquille	$Q_{est} = 0.06 * A_{plume} + 0.28 * L_m - 7.66 * Tides$
Rogue	$Q_{est} = 0.05 * A_{plume} + 0.49 * L_m$
Siuslaw	$Q_{est} = 0.17 * A_{plume} + 0.02 * L_m$

Table 17: Final multiple linear regression models statistics of the four rivers based on the manual method

River Name	R2	Adj R2	p-value	Final Model
Chetco	0.65	0.64	$3.67 * 10^{-8}$	$Q_{est} \sim A_{plume} + L_m + Angle$
Coquille	0.64	0.61	$1.02 * 10^{-9}$	$Q_{est} \sim A_{plume} + L_m + Tides$
Rogue	0.59	0.58	$2.20 * 10^{-9}$	$Q_{est} \sim A_{plume} + L_m$
Siuslaw	0.66	0.61	$1.74 * 10^{-4}$	$Q_{est} \sim A_{plume} + L_m$

We regressed $Q_{estimated}$ values v/s $Q_{measured}$ values to evaluate models and we compared slope and intercept parameters against the 1:1 line to describe the consistency and the model bias respectively.

Table 18 and Figures 19, 20, 21 and 22 show the regression line of estimated and measured discharges with the corresponding R^2 coefficient for each river. Because no discharge rate should be estimated when no discharge rate is measured, i.e. there is no physical meaning, the intercept is forced to be zero. From below results, we can see that the obtained regression lines represent generally around 90% of the measured discharges with an acceptable R^2 values around 0.5.

Table 18: Estimated discharges v/s measured discharges linear regression lines of the four rivers.

	Chetco	Coquille	Rogue	Siuslaw
Regression Line	$y = 0.86x$	$y = 0.87x$	$y = 0.89x$	$y = 0.93x$
R2	0.54	0.55	0.39	0.52

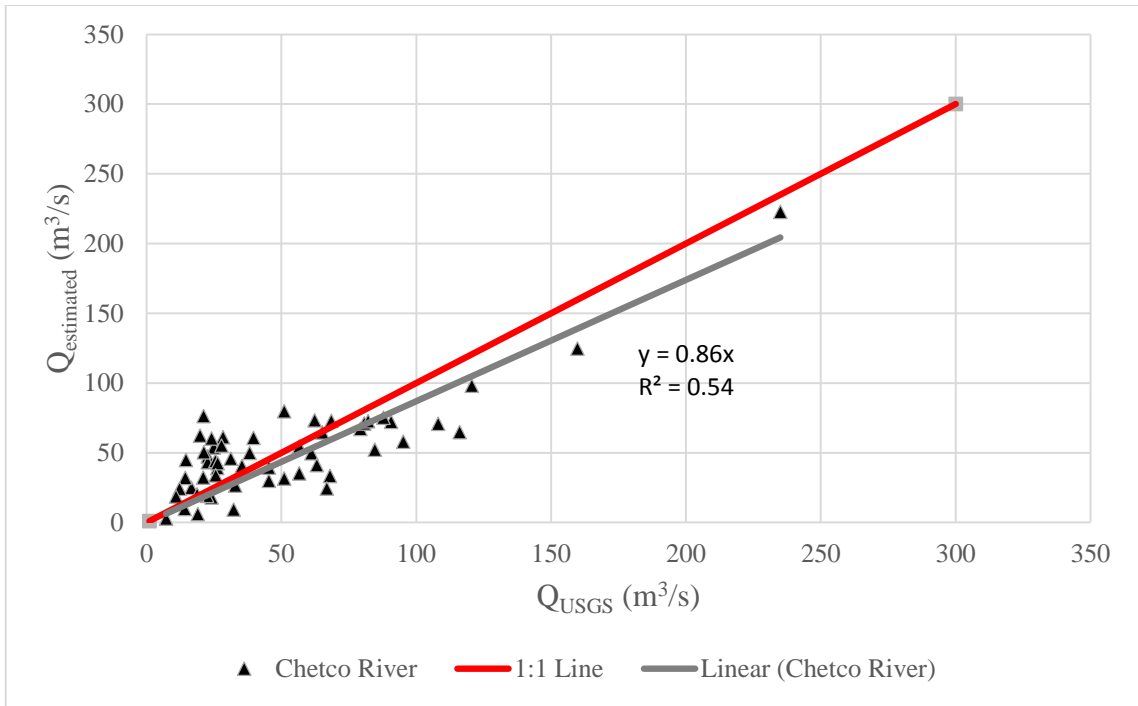


Figure 19: Scatter plot of $Q_{\text{estimated}}$ (m^3/s) from the linear regression model and Q_{USGS} (m^3/s) from the USGS dataset for Chetco River ($y = 0.86x$) and the 1:1 line in red.

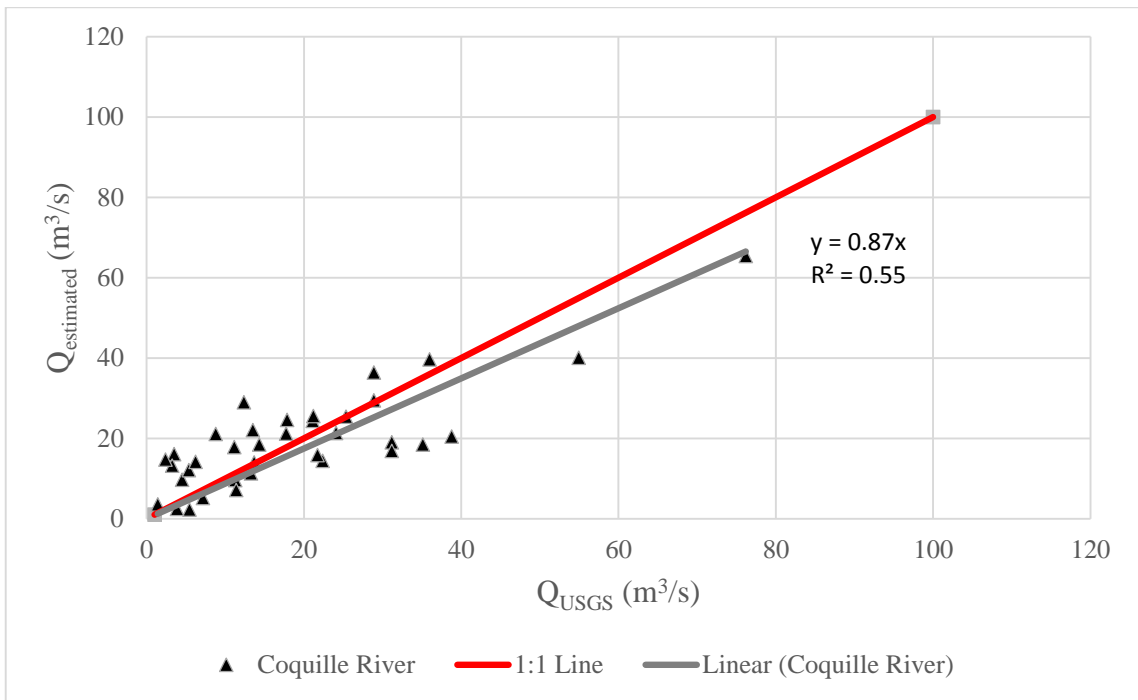


Figure 20: Scatter plot of $Q_{\text{estimated}}$ (m^3/s) from the linear regression model and Q_{USGS} (m^3/s) from the USGS dataset for Coquille River ($y = 0.87x$) and the 1:1 line in red.

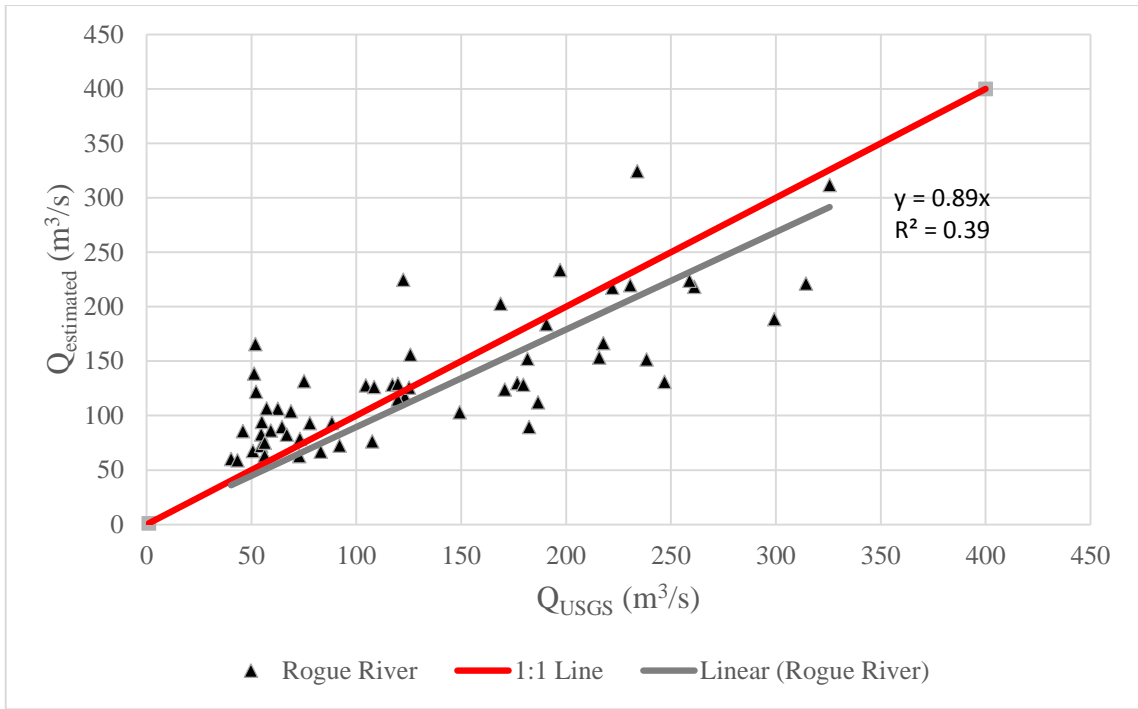


Figure 21: Scatter plot of $Q_{\text{estimated}}$ (m³/s) from the linear regression model and Q_{USGS} (m³/s) from the USGS dataset for Rogue River ($y = 0.89x$) and the 1:1 line in red.

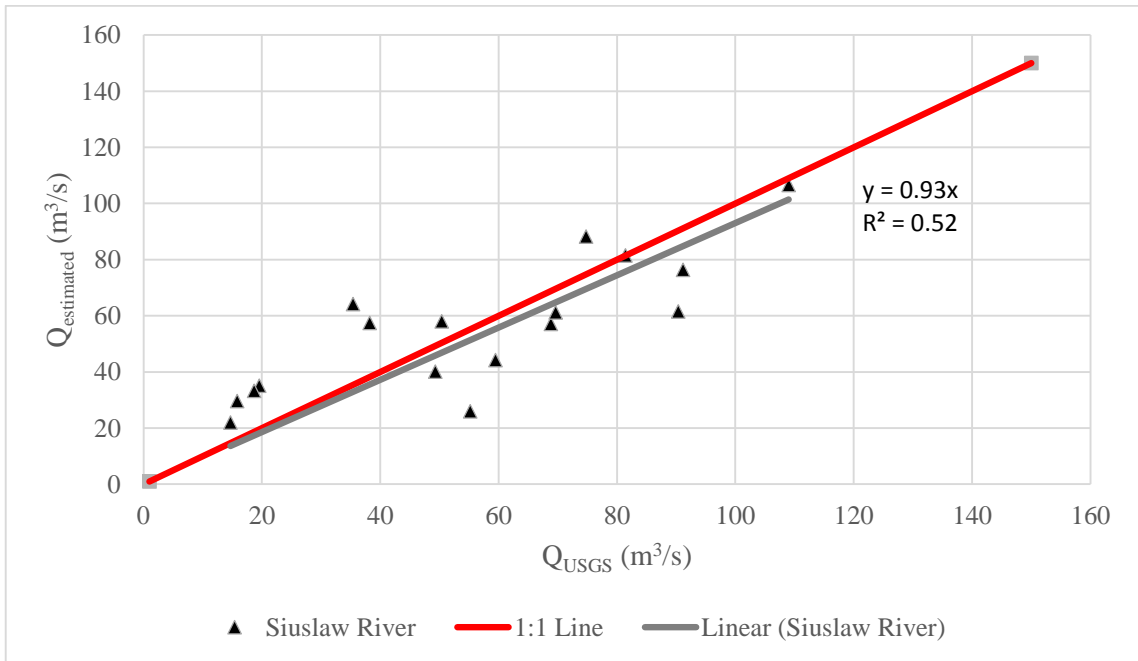


Figure 22: Scatter plot of $Q_{\text{estimated}}$ (m³/s) from the linear regression model and Q_{USGS} (m³/s) from the USGS dataset for Siuslaw River ($y = 0.93x$) and the 1:1 line in red.

We then assessed the residuals through the diagnostic plots shown in Appendices B,C,D and E below to check whether the linear regression assumptions are met and to improve the models in an explanatory way.

The diagnostic plots show residuals in four different ways. For the first plot in every model is the **Residuals vs Fitted** plot in which we evaluated if the residuals have non-linear patterns. For the four models, residuals spread around a horizontal line without distinct patterns which indicating that we do not have non-linear relationships.

The second plot called **Normal Q-Q** plot show if residuals are normally distributed. The plots show that residuals follow the 1:1 line well and do not deviate severely and thus normality assumption is verified.

The third plot **Scaled-Location** shows if residuals are spread equally along the range of predictors to check if the error term is the same across all values of the independent variables. A horizontal line with equally randomly spread points verify the assumption. No distinctive pattern is observed except for Chetco River where a small deviation non-informative from the horizontal line is noticed.

The final plot is the **Residuals v/s Leverage**. This plot shows the influential cases where outlying values are observed at the upper right corner or at the lower right corner. Points outside the red lines indicating the Cook's distance are influential to the regression results. No danger points with Cook's distance greater than 1 are located for any river.

Afterwards, both statistical and graphical model evaluation techniques (RMSE, RSR, NSE and PBIAS) as described in section F were measured. Results of these parameters are summarized in Table 19 below. Table 20 reports the performance rating of these statistical parameters.

Table 19: Summary of reported RMSE, RSR, NSE and PBIAS values from the rivers final models.

River	RMSE	RSR	NSE	PBIAS (%)
Chetco	28.01	0.61	0.64	0.57
Coquille	19.36	0.58	0.66	3.14
Rogue	51.27	0.64	0.57	5.62
Siuslaw	18.02	0.59	0.64	3.10

Table 20: Reported performance rating of the statistical parameters (RSR, NSE and PBIAS)

Performance Rating	RSR	NSE	PBIAS (%)
Very Good	$0 \leq \text{RSR} \leq 0.5$	$0.75 < \text{NSE} \leq 1$	$\text{PBIAS} \leq \pm 10$
Good	$0.5 \leq \text{RSR} \leq 0.6$	$0.65 \leq \text{NSE} \leq 0.75$	$\pm 10 \leq \text{PBIAS} \leq \pm 15$
Satisfactory	$0.6 \leq \text{RSR} \leq 0.7$	$0.5 \leq \text{NSE} \leq 0.65$	$\pm 15 \leq \text{PBIAS} \leq \pm 25$
Unsatisfactory	$\text{RSR} > 0.7$	$\text{NSE} \leq 0.5$	$\text{PBIAS} \geq \pm 25$

We then assessed the prediction's ability of each model by applying the k-fold cross validation method. Cross-validation is a model validation technique for assessing how the results of a statistical analysis will generalize to an independent data set. K-fold is a technique widely used for estimating the test error. Estimates are used to give an idea of the test error of the final chosen model. The idea is to randomly divide the data into k equal-sized parts. We leave out part k, fit the model to the other k-1 parts (combined), and then obtain predictions for the left-out kth part.

The 4-fold cross validation was conducted and repeated 5 times. The error on each of the predictions is recorded and the average of the four-recorded errors, called the cross-validation error is reported and will serve as the performance metric for the model. The cross-validations plots are illustrated in below Appendices II, III, IV and V with respectively an overall mean square error of 600, 146, 2180, 296 for Chetco, Coquille, Rogue and Siuslaw rivers.

The predictive squared correlation coefficient Q^2 is calculated for each model to assess the model prediction power. Close Q^2 values to R^2 indicate a no over-fitting model and a high model predication power. Here below Table 21 show the results of the model prediction power calculations.

Table 21: Summary of cross validation assessment and model prediction power calculations.

	Chetco	Coquille	Rogue	Siuslaw
Elements	56	36	57	17
MODEL CALIBRATION (LR)				
mean (observed)	42.147	20.054	123.987	58.701
mean (predicted)	42.147	20.054	123.987	58.701
rmse (nu = 0)	22.017	8.860	50.035	16.392
R ²	0.621	0.616	0.575	0.604
PREDICTION PERFORMANCE (CV)				
Runs	5	5	5	5
Groups	4	4	4	4
Elements Training Set	42	27	42 (+1)	12 (+1)
Elements Test Set	14	9	15 (-1)	5 (-1)
mean (observed)	42.147	20.054	123.987	58.701
mean (predicted)	42.021	19.937	125.377	57.116
rmse (nu = 1)	23.774	9.979	57.365	24.705
Q ²	0.581	0.576	0.511	0.583

As a result of the diagnostic plots and verification of the models we can conclude that the linearity assumption of the models is checked and verified for the four rivers. Normality assumption is also verified with small deviation in the lower and upper quantile of each model. Low discharge rates are characterized by a low initial momentum ; thus, the plume is subject to deviation and deformation caused by the tides, winds and surface currents near shoreline (Jones et al., 2007).

The linear regression model of the four rivers reveals the important correlation between the discharge rate, the plume area and the length scale. This correlation reconcile the results found also by (Burrage et al., 2008; Cole & Hetland, 2016; Coynel et al., 2005).

On the other hand, the models show no significant correlation with the tides mean level for all three rivers Chetco, Rogue and Siuslaw except for Coquille River. The results go well with the findings of (Ming Li & Zengrui Rong, 2012) who investigated the effects of the tides on the Changjiang River plume and found that in the presence of tides, the plume is moved in the directions of tidal currents thus increasing the downstream freshwater transport. One explanation could be the relatively low discharge

rates of Coquille River ($Q_{\text{mean}} = 22 \text{ m}^3/\text{s}$) compared to the other rivers ($Q_{\text{mean}} = 64 \text{ m}^3/\text{s}$ for Chetco, $Q_{\text{mean}} = 162 \text{ m}^3/\text{s}$ for Rogue and $Q_{\text{mean}} = 180 \text{ m}^3/\text{s}$ for Siuslaw). These low discharge rates lead to a weak stability of the plumes towards the tidal currents in the vicinity area of Coquille River mouth and a shallower plumes easier to transport by the tides.

The partial regression coefficients of L_m and A_{plume} are positively correlated with the flow river. The range for A_{plume} coefficients is between 0.05 and 0.17. For rivers with lower discharge rates, the partial coefficients are higher than the other rivers. Moreover, L_m values are more correlated with the discharge rate for Rogue and Coquille than for Chetco and Siuslaw Rivers. The negative coefficient related to Coquille River indicates an inverse proportional relationship between the river discharge rate and the tides, i.e. when the tides level is high the discharge rate is low and vice versa.

Furthermore, Turbidity created by relatively high discharge rate ($> 50 \text{ m}^3/\text{s}$) and high temperature gradient between ocean water temperature and river temperature ($\Delta > 2.5$), enhance the mixing process which redefine the interaction between the plume and thus the temperature profile of the plume is distorted (Robert D. Hetland, 2005; Ming Li & Zengrui Rong, 2012), especially when the deviation of the plume is noticed as remarked in LE70470311999353EDC, LE70460312000029EDC and LE70460312003005EDC images for example for Rogue River.

Other remarkable identifications during this study are important to mention; winter plumes have generally a small temperature gradient unlike spring/late autumn plumes which temperature gradient can go up to 5-6 K. Because of these high gradients, spring plumes can be detected at lower discharge rates but unfortunately clouds during this period are much more located in the coastline area than in winter season. Moreover,

because of lower discharge, which values depend on the river characteristics but generally around $10 \text{ m}^3/\text{s}$, plumes tend to deviate easily, as their momentum jet is lower, toward the shoreline. These images are not taken into consideration as their behavior is very complex to study as well as their delineation.

CHAPTER V

DISCUSSION AND CONCLUSION

In this study, we present a new method of estimating river discharge using Landsat 7 ETM+ satellite imagery. The utility of remote-sensing-based measurement of river plume characteristics is increasingly recognized for quantifying transported freshwater and applications for hydrodynamic modelling ([Fernandez et al., 2014](#); [Klemas, 2011](#); [Osadchiev, 2015](#); [Ou et al., 2009](#)). The general idea of this method is a conversion of satellite-derived thermal properties of river plumes in the sea into information about the river discharge.

The accuracy of the discharge estimates reported in Table 19 indicate that these estimates can be successfully developed from imagery information (plume area A_{plume} , length scale L_m , deviation angle of the plume from river mouth centerline θ and tides mean water level T_L). The mean accuracy of the estimates can be expected to be within 60% (Table 15) of the observed discharge.

This level of accuracy suggests that remote estimates of discharge would be most useful in regional or continental scale studies where the accuracy of the aggregate is more important than at specific locations, or where data is lacking and an estimate with a known range of expected error would enable quantification of discharge within a statistical framework especially for ungauged rivers and streams in many part of the world.

Moreover, the advantage of this approach compared to other remotely sensed methods stated in the introduction ([Birkinshaw et al., 2014](#); [Bjerklie et al., 2005](#)) lies in the fact that most commonly used satellite sensors cannot resolve small size rivers, but

can report more easily the buoyant plumes formed by these rivers. The proposed method can be used to evaluate freshwater discharges from small rivers with relatively narrow riverbeds and complex watershed systems where other indirect methods (based on hydrological assumptions and manning calculations) encounter substantial difficulties.

However, some limitations of this approach are to be mentioned. At first, the application of this method is restricted to rivers with two jetties river-mouth configuration. Similarly to the studied rivers, the method was applied to two rivers with barrier spits formation at the river mouth location (Smith and Klamath rivers in California) and the accuracy of the flow estimates was about 10% of the observed discharge rates. In addition to that, the magnitude of the atmospheric effect will depend on the water vapor content of the intervening atmosphere. This unknown or uncertain atmospheric contribution is one of the problems for the remote sensing of surface temperature at infrared wavelengths. Thus, advanced atmospheric correction based on available meteorological data at the image acquisition time will help generate a more accurate surface temperatures.

Moreover, the presented method strongly relies on the availability and quality of satellite imagery. Firstly, it cannot be used during ice coverage periods as river plumes are formed under the ice sheet, inhibiting their detection by remote sensing means and thus for the rivers in the upstream side of the northern hemisphere. Secondly, the cloud coverage reduce the optical satellite images quality and availability. In the case of Oregon state, most images captured during winter season, where the flow rate is at its maximum, are approximately 70% covered by cloud that impede their utilization.

However, this problem could be overcome using non-optical satellite products that do not depend on cloud coverage, for instance SAR products, which also have a very good spatial resolution but are more costly.

In addition to that, the resolution of the thermal imagery is insufficient to assess the near field region independently of the much larger expanse of the far field plume. Future work could investigate methods to characterize and estimate the far field area for more precise results.

Furthermore, accurate delimitation of the fields by comparing the thermal plume areas to suspended solid areas or plumes dynamic areas could enhance the model. Improved spatial and spectral characteristics in advanced satellites such as Landsat 8 (16-bit with 55,000 grey levels instead of 256 levels of Landsat 7) will allow for more accurate characterization of spatial variability in plume form, more precision in geometric properties delineation of the formed area and a more understanding of the river-ocean interaction, thus a more accurate estimation of the river discharge rate.

Besides, the acquisition frequency of the Landsat imagery (1 pass every 16 days) affect the satellite image in term of availability. The usage of satellites with enhanced temporal resolutions of the data permit a precise categorization of the images based on the season and thus can be used not only for a general estimation but also for the evaluation of the seasonal variability (autumn, winter and spring).

BIBLIOGRAPHY

- Barrett, E. (1998). Satellite remote sensing in hydrometry *Hydrometry: Principles and Practices* (pp. 199-224). Chichester: second ed. Wiley.
- Barsi, J. A., Barker, J. L., & Schott, J. R. (2003). *An atmospheric correction parameter calculator for a single thermal band earth-sensing instrument*. Paper presented at the Geoscience and Remote Sensing Symposium, 2003. IGARSS'03. Proceedings. 2003 IEEE International.
- Birkett, C. M., Mertes, L. A. K., Dunne, T., Costa, M. H., & Jasinski, M. J. (2002). Surface water dynamics in the Amazon Basin: application of satellite radar altimetry. *Journal of Geophysical Research*, *107*, 8059.
- Birkinshaw, S., Moore, P., Kilsby, C., O'Donnell, G., Hardy, A., & Berry, P. (2014). Daily discharge estimation at ungauged river sites using remote sensing. *Hydrological Processes*, *28*(3), 1043-1054.
- Bjerklie, D. M., Moller, D., Smith, L. C., & Dingman, S. L. (2005). Estimating discharge in rivers using remotely sensed hydraulic information. *Journal of Hydrology*, *309*(1), 191-209.
- Burrage, D., Wesson, J., Martinez, C., Perez, T., Moller, O., & Piola, A. (2008). Patos lagoon overflow within the Rio de la Plata plume using an airborne salinity mapper: observing an embedded plume. *Continental Shelf Research*, *28*(13), 1625-1638.
- Cannizzaro, J. P., Carlson, P. R., Yarbrow, L. A., & Hu, C. (2013). Optical variability along a river plume gradient: Implications for management and remote sensing. *Estuarine, Coastal and Shelf Science*, *131*, 149-161.
- Chen, F., & MacDonald, D. G. (2006). Role of mixing in the structure and evolution of a buoyant discharge plume. *Journal of Geophysical Research: Oceans*, *111*(C11).
- Chen, F., MacDonald, D. G., & Hetland, R. D. (2009). Lateral spreading of a near - field river plume: Observations and numerical simulations. *Journal of Geophysical Research: Oceans*, *114*(C7).
- Chen, J. (2011). A simple and effective method for filling gaps in Landsat ETM+ SLC-off images. *Remote Sensing of Environment*, 1-12.
- Cole, K. L., & Hetland, R. D. (2016). The Effects of Rotation and River Discharge on Net Mixing in Small-Mouth Kelvin Number Plumes. *Journal of Physical Oceanography*, *46*(5), 1421-1436.
- Coyne, A., Seyler, P., Etcheber, H., Meybeck, M., & Orange, D. (2005). Spatial and seasonal dynamics of total suspended sediment and organic carbon species in the Congo River. *Global Biogeochem. Cycles*.
- Dinnel, S. P., Schroeder, W. W., & Wiseman Jr, W. J. (1990). Estuarine-shelf exchange using Landsat images of discharge plumes. *Journal of Coastal Research*, 789-799.

- Enjolras, V., Vincent, P., Souyris, J.-C., Rodriguez, E., Phalippou, L., & Cazenave, A. (2006). Performances study of interferometric radar altimeters: from the instrument to the global mission definition. *Sensors*, 6(3), 164-192.
- Fernandez, R., Bonansea, M., & Marques, M. (2014). Monitoring turbid plume behavior from landsat imagery. *Water resources management*, 28(10), 3255-3269.
- Garvine, R. W. (1995). A dynamical system for classifying buoyant coastal discharges. *Continental Shelf Research*, 15(13), 1585-1596.
- Garvine, R. W. (1995). A dynamical system for classifying buoyant coastal discharges. *Continental Shelf Research*, 15, 1585-1596.
- Hetland, R. D. (2005). Relating river plume structure to vertical mixing. *Journal of Physical Oceanography*, 35(9), 1667-1688.
- Hetland, R. D., & MacDonald, D. G. (2008). Spreading in the near-field Merrimack River plume. *Ocean Modelling*, 21(1), 12-21.
- Hirpa, F. A., Hopson, T. M., De Groeve, T., Brakenridge, G. R., Gebremichael, M., & Restrepo, P. J. (2013). Upstream satellite remote sensing for river discharge forecasting: Application to major rivers in South Asia. *Remote Sensing of Environment*, 131, 140-151.
- Jabbar, A., Lihan, T., Mustapha, M. A., Rahman, Z. A., & Rahim, S. (2013). Variability of river plume signature determined using satellite images. *Journal of Applied Sciences*, 13(1), 70.
- Jirka, G. H., Adams, E. E., & Stolzenbach, K. D. (1981). Buoyant surface jets. *Journal of Hydraulics Division ASCE*, 1467-1487.
- Johnson, D. R., Miller, J., & Schofield, a. O. (2003). Dynamics and optics of the Hudson River outflow plume. *J. Geophys. Res.*, 108(C10), 3323.
- Johnson, D. R., Miller, J., & Schofield, O. (2003). Dynamics and optics of the Hudson River outflow plume. *Journal of Geophysical Research: Oceans*, 108(C10).
- Jones, G. R., Nash, J. D., Doneker, R. L., & Jirka, G. H. (2007). Surface Discharges into Water Bodies. I: Flow Classification and Prediction Methodology. *Journal of Hydraulic Engineering*, 1021-1036.
- Kaufman, J. T., & Adams, E. E. (1981). *Coupled Near and Far Field Thermal Plume Analysis Using Finite Element Techniques*. Retrieved from Cambridge, Massachusetts:
- Kaya, S., Seker, D. Z., Kabdasli, S., Musaoglu, N., Yuasa, A., & Shrestha, M. B. (2006). Monitoring turbid freshwater plume characteristics by means of remotely sensed data. *Hydrological Processes*, 20(11), 2429-2440.
- Klemas, V. (2011). Remote sensing of coastal plumes and ocean fronts: overview and case study. *Journal of Coastal Research*, 28(1A), 1-7.
- Li, M., & Rong, Z. (2012). Effects of tides on freshwater and volume transports in the Changjiang River plume. *Journal of Geophysical Research: Oceans*, 117(C6).
- Li, M., & Rong, Z. (2012). Effects of tides on freshwater and volume transports in the Changjiang River plume. *Journal of Geophysical Research*, 6, 117.

- Lo, C. P., & Yang, X. (1998). *Some Practical considerations of relative radiometric normalization of multirate Landsat MSS data for land use detection*. Paper presented at the Proceedings of ASPRS/RTI 1998 Annual Convention, Tampa, Florida.
- Markham, B. L., Barker, J. L., Barsi, J. A., Kaita, E., Thome, K. J., Helder, D. L., . . . Scaramuzza, P. (2003). Landsat-7 ETM+ radiometric stability and absolute. *Sensors, Systems, and Next-Generation Satellites VI 4881*, 308-318.
- Miller, Z. F., Pavelsky, T. M., & Allen, G. (2014). Quantifying river form variations in the Mississippi Basin using remotely sensed imagery. *Hydrology and Earth System Sciences*, 18(12), 4883-4895.
- Mustard, J., Carney, M., & Sen, A. (1999). The use of satellite data to quantify thermal effluent impacts. *Estuarine, Coastal and Shelf Science*, 49(4), 509-524.
- Natural Resources of Chetco Estuary*. (1979). Retrieved from Oregon:
- NOAA. (2015). *NOAA Tide Predictions: Brookings, Chetco cove, Oregon*. Retrieved from Brookings:
- Osadchiv, A. (2015). A method for quantifying freshwater discharge rates from satellite observations and Lagrangian numerical modeling of river plumes. *Environmental Research Letters*, 10(8), 085009.
- Ou, S., Zhang, H., & Wang, D.-x. (2009). Dynamics of the buoyant plume off the Pearl River Estuary in summer. *Environmental fluid mechanics*, 9(5), 471-492.
- Siuslaw River Jetty Extension*. (1976). Retrieved from Portland:
- Sun, W., Ishidaira, H., & Bastola, S. (2010). Towards improving river discharge estimation in ungauged basins: calibration of rainfall-runoff models based on satellite observations of river flow width at basin outlet. *Hydrology and Earth System Sciences*, 14(10), 2011-2022.
- Thomas, A., Byrne, D., & Weatherbee, R. (2002a). Coastal sea surface temperature variability from Landsat infrared data. *Remote Sensing of Environment*, 81(2), 262-272.
- Thomas, A., Byrne, D., & Weatherbee, R. (2002b). Coastal sea surface temperature variability from Landsat infrared data. *Remote Sensing of Environment*, 81(2), 262-272.
- Tilburg, C. E., Gill, S. M., Zeeman, S. I., Carlson, A. E., Arienti, T. W., Eickhorst, J. A., & Yund, P. O. (2011). Characteristics of a shallow river plume: observations from the Saco River Coastal Observing System. *Estuaries and Coasts*, 34(4), 785-799.
- Walker, N. D., Jr, W. J. W., Jr, L. J. R., & Babin., a. A. (2005). Effects of river discharge, wind stress, and slope eddies on circulation and the satellite-observed structure of the mississippi river plume. *Journal of Coastal Research*, 21(6), 1228-1244.
- Wloczyk, C., Richter, R., Borg, E., & Neubert, W. (2006). Sea and lake surface temperature retrieval from Landsat thermal data in Northern Germany. *International Journal of Remote Sensing*, 2489-2502.

- Yang, L., Huang, C., Homer, C. G., Wylie, B. K., & Coan, M. J. (2003). An approach for mapping large-area impervious surfaces: synergistic use of Landsat-7 ETM+ and high spatial resolution imagery. *Canadian Journal of Remote Sensing*, 29(2), 230-240.
- Yankovsky, A. E., & Chapman, D. C. (1997). A simple theory for the fate of buoyant coastal discharges*. *Journal of Physical Oceanography*, 27(7), 1386-1401.

APPENDICES

I. Multicollinearity diagnostics results

Table A 1: VIFs results for the multicollinearity diagnostics of the four rivers models

River	Tested Var	Var_1	Var_2	Var_3
Chetco	A _{near}	L _m	Angle	Tides
	-	1.03	1.03	1.01
	L _m	A _{near}	Angle	Tides
	-	1.05	1.05	1.01
	Angle	L _m	A _{near}	Tides
	-	1.22	1.21	1.01
	Tides	L _m	A _{near}	Angle
	-	1.31	1.33	1.12
Coquille	A _{near}	L _m	Angle	Tides
	-	1.26	1.01	1.25
	L _m	A _{near}	Angle	Tides
	-	1.08	1.03	1.06
	Angle	L _m	A _{near}	Tides
	-	1.73	1.46	1.25
	Tides	L _m	A _{near}	Angle
	-	1.54	1.55	1.08
Rogue	A _{near}	L _m	Angle	Tides
	-	1.25	1.30	1.06
	L _m	A _{near}	Angle	Tides
	-	1.04	1.08	1.06
	Angle	L _m	A _{near}	Tides
	-	1.09	1.09	1.01
	Tides	L _m	A _{near}	Angle
	-	1.32	1.08	1.25
Siuslaw	A _{near}	L _m	Angle	Tides
	-	1.26	1.32	1.16
	L _m	A _{near}	Angle	Tides
	-	1.12	1.26	1.16
	Angle	L _m	A _{near}	Tides
	-	1.08	1.00	1.08
	Tides	L _m	A _{near}	Angle
	-	1.26	1.11	1.37

II. CHETCO RIVER MODEL ASSESSMENT PLOTS

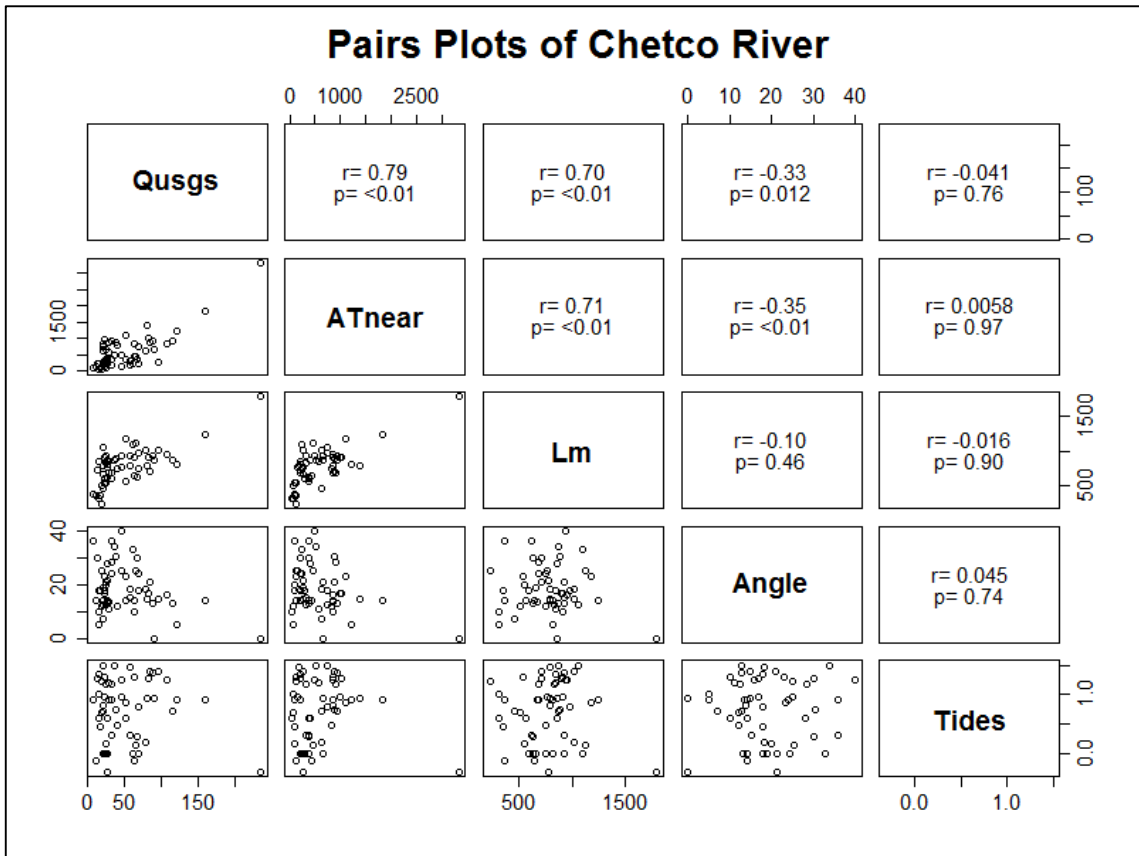


Figure-B. 1: Chetco River: Pair-wise scatter plots of predictors and independent variable (QUSGS) with correlation (range: -1 to 1) and p-values with best correlation close to -/+ 1 for p-value < 0.1

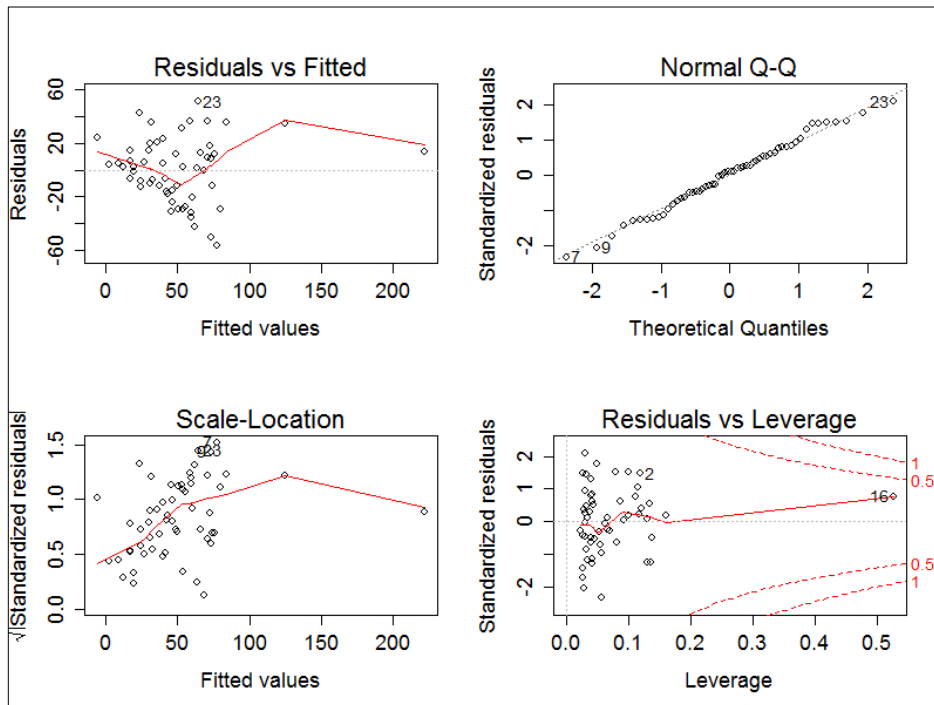


Figure-B. 2: Chetco River linear model diagnostic plots

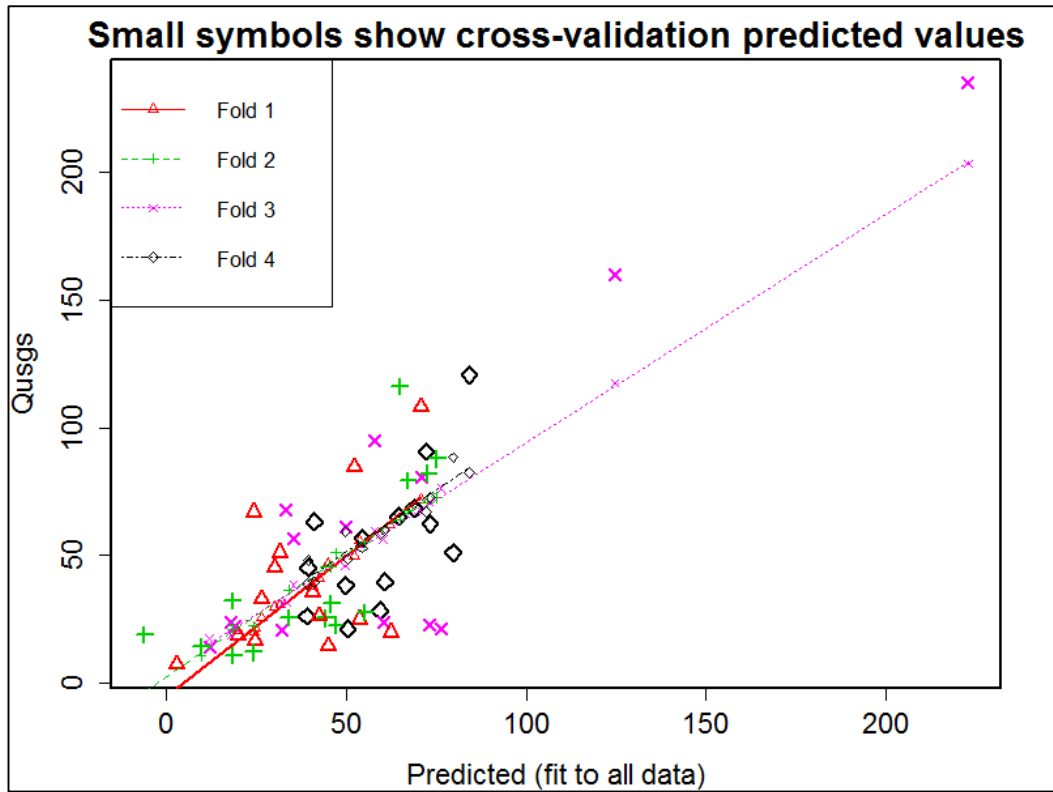


Figure-B. 3: Chetco River Cross Validation-Overall Mean Square 611

III. COQUILLE RIVER MODEL ASSESSMENT PLOTS

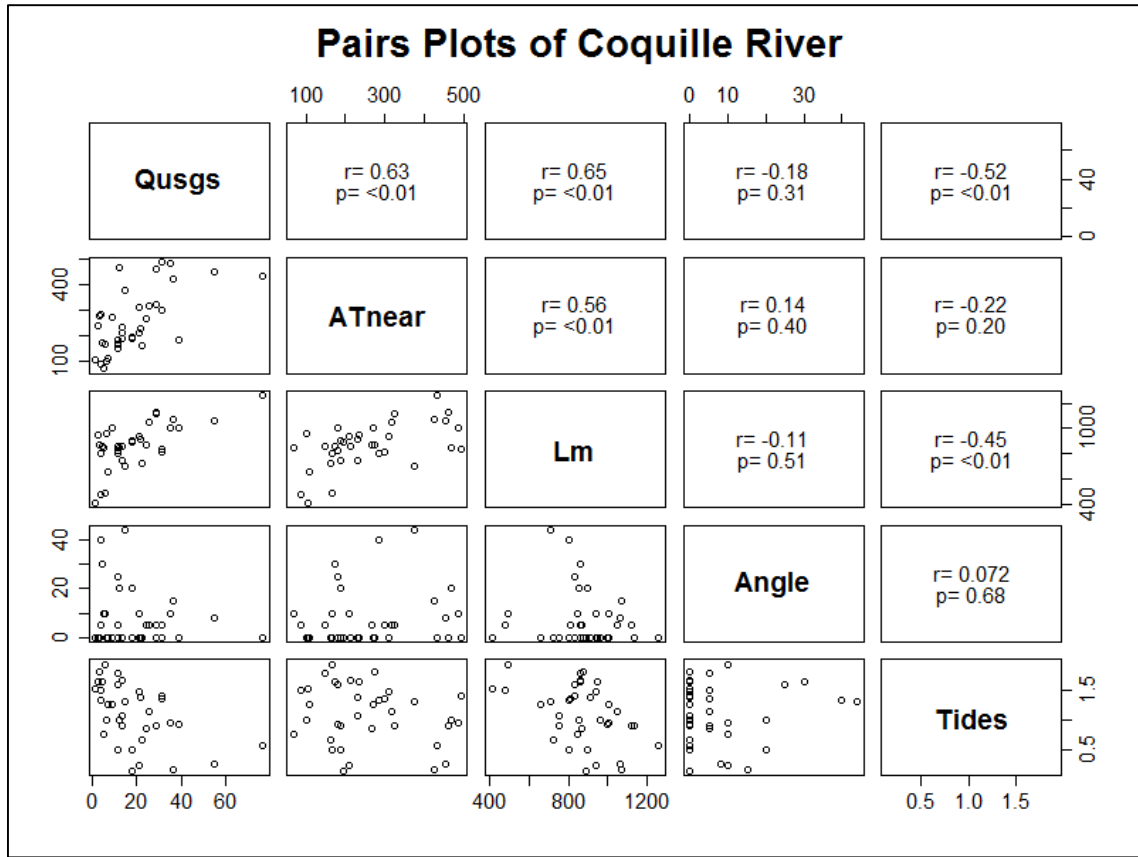


Figure-C. 1: Coquille River: Pair-wise scatter plots of predictors and independent variable (Q_{USGS}) with correlation (range: -1 to 1) and p-values with best correlation close to +/- 1 for p-value <0.1

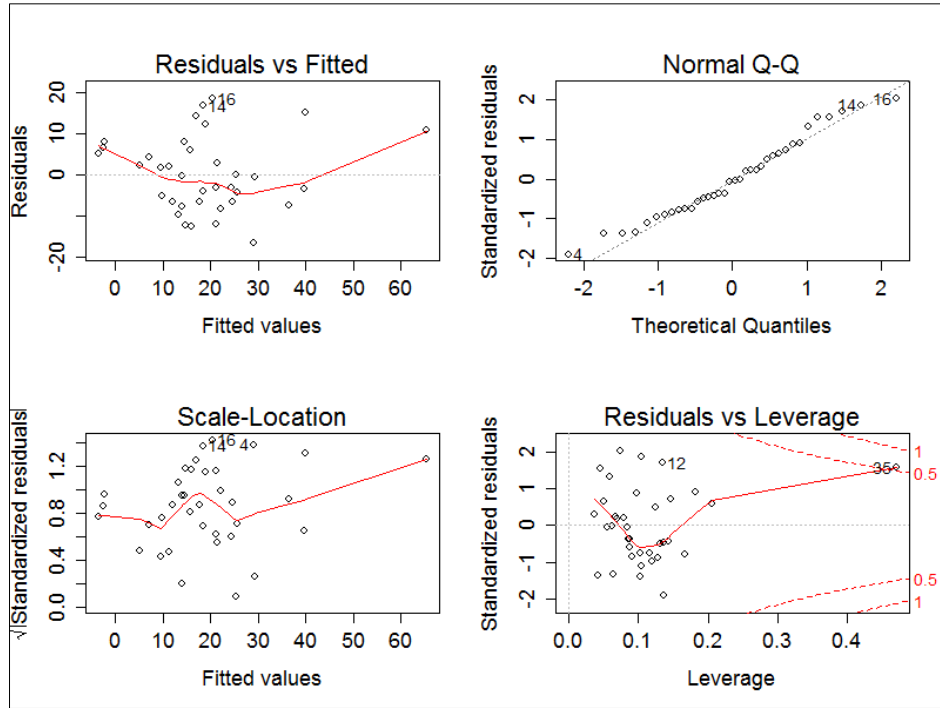


Figure-C. 2: Coquille River linear model diagnostic plots

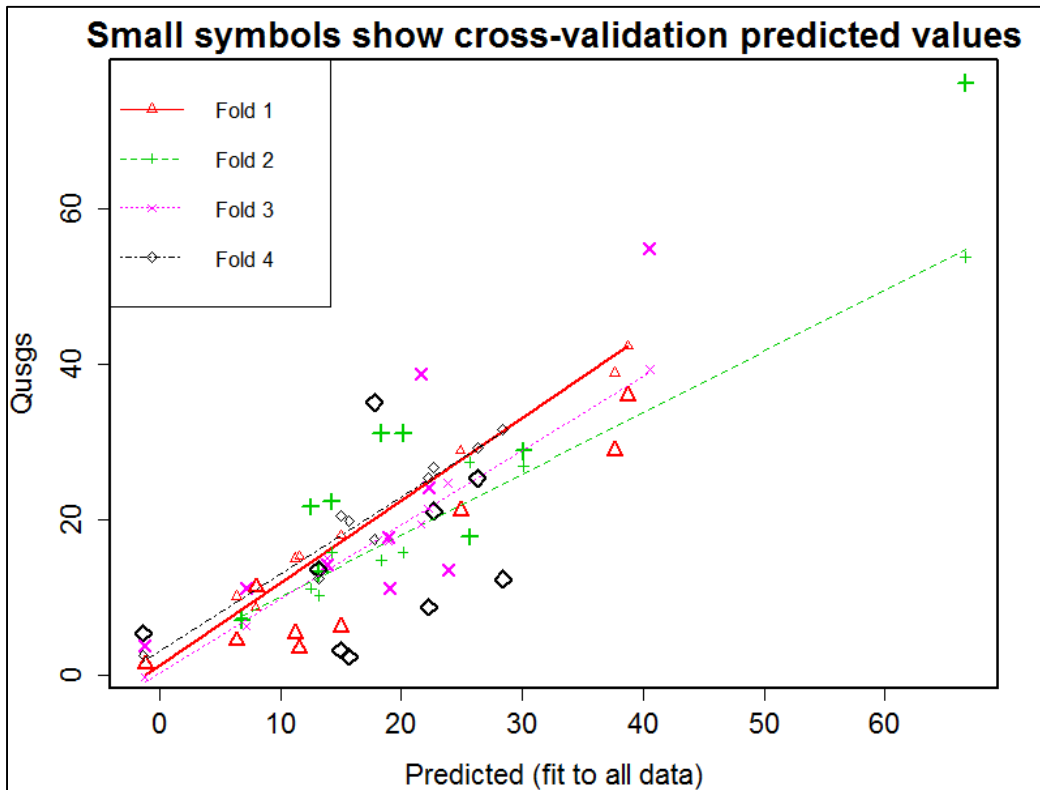


Figure-C. 3: Coquille River Cross Validation-Overall Mean Square 146

IV. ROGUE RIVER MODEL ASSESSMENT PLOTS

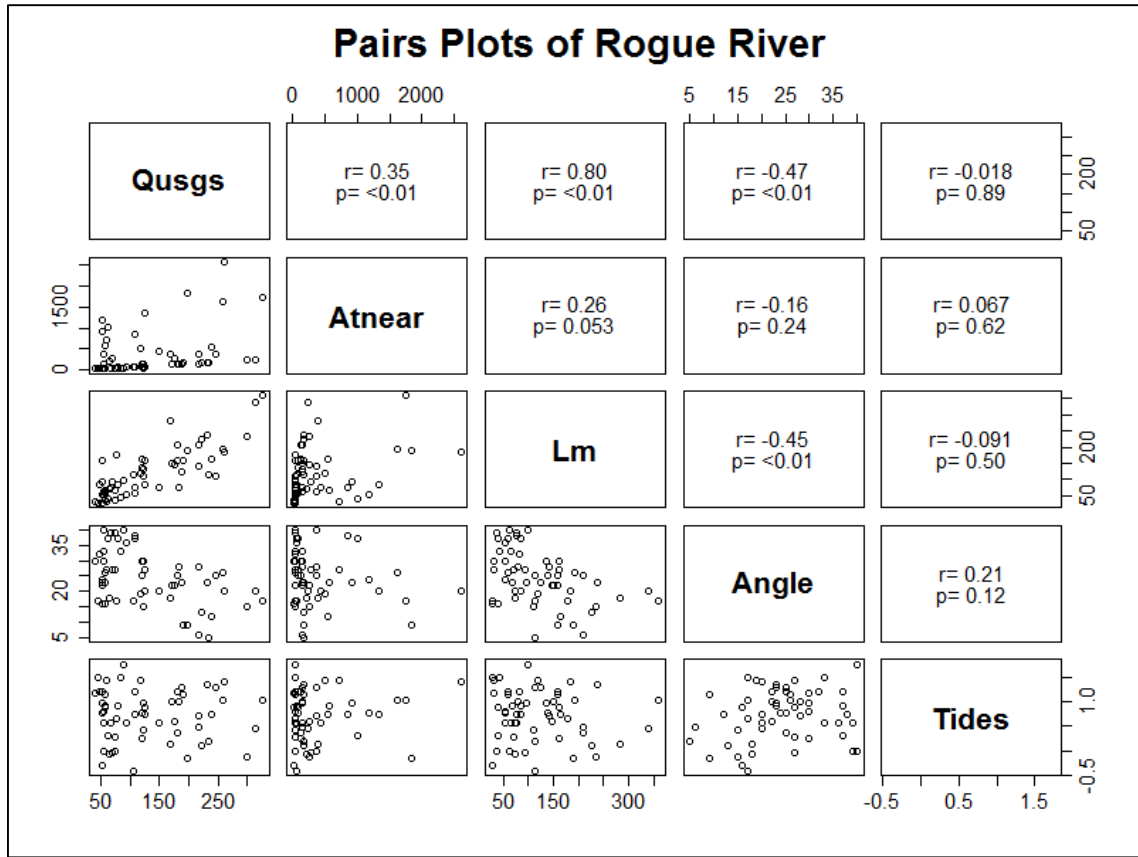


Figure-D. 1: Rogue River: Pair-wise scatter plots of predictors and independent variable (Q_{USGS}) with correlation (range: -1 to 1) and p-values with best correlation close to ± 1 for p-value < 0.1

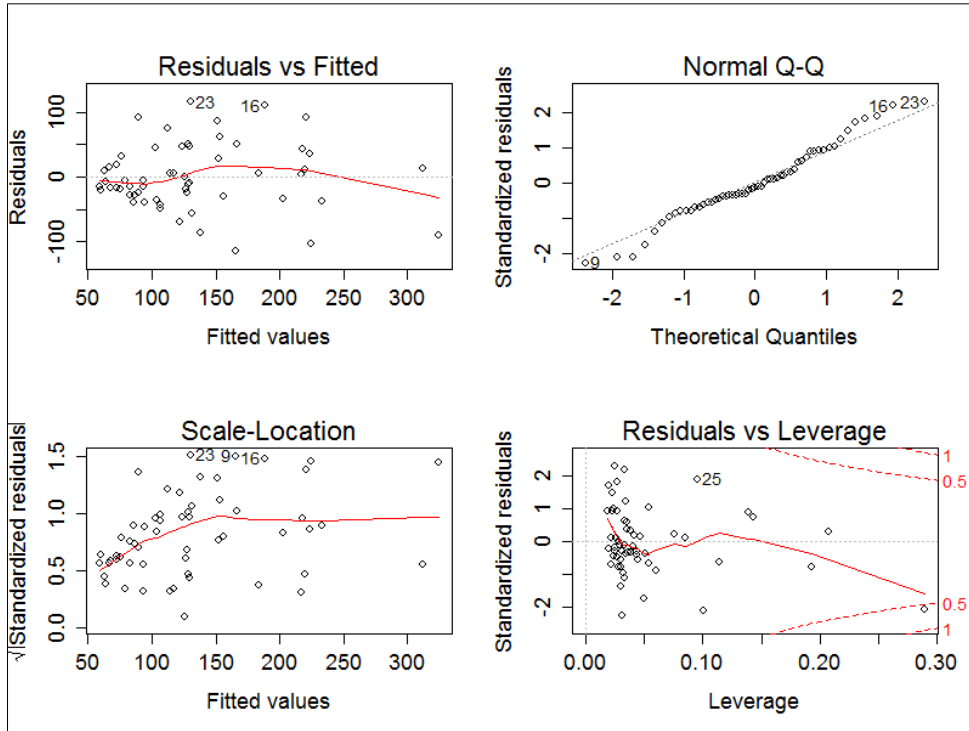


Figure-D. 2: Rogue River linear model diagnostic plots

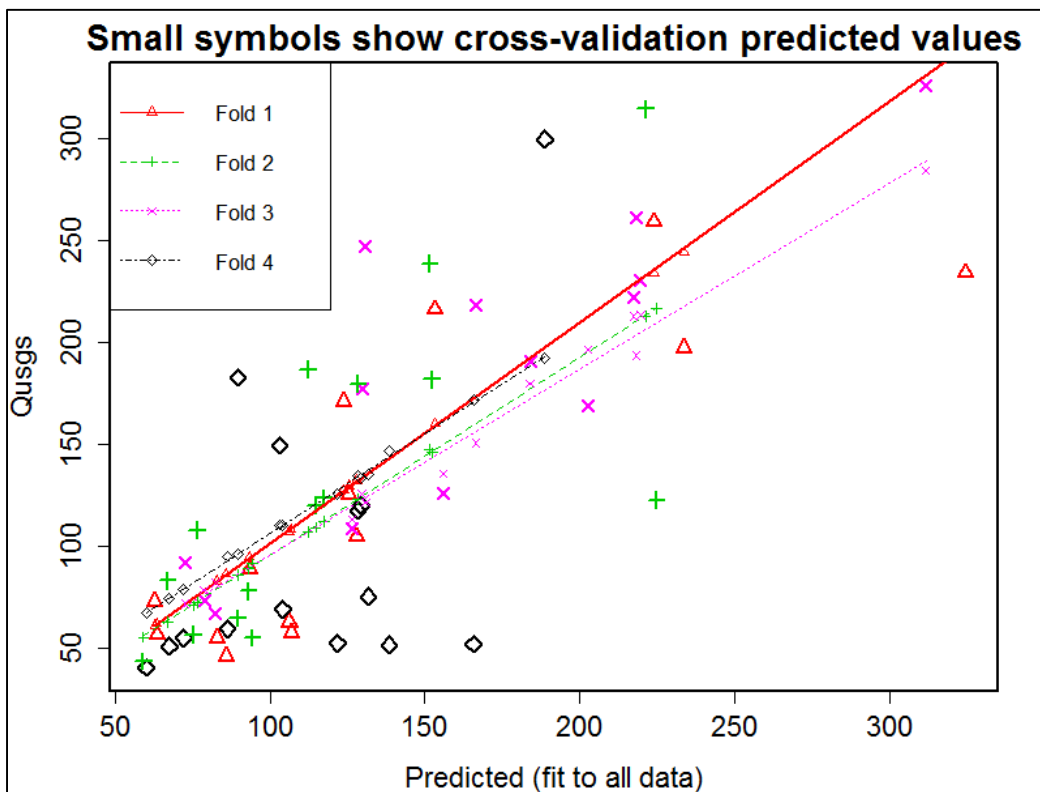


Figure-D. 3: Rogue River Cross Validation-Overall Mean Square 2180

v. SIUSLAW RIVER MODEL ASSESSMENT PLOTS

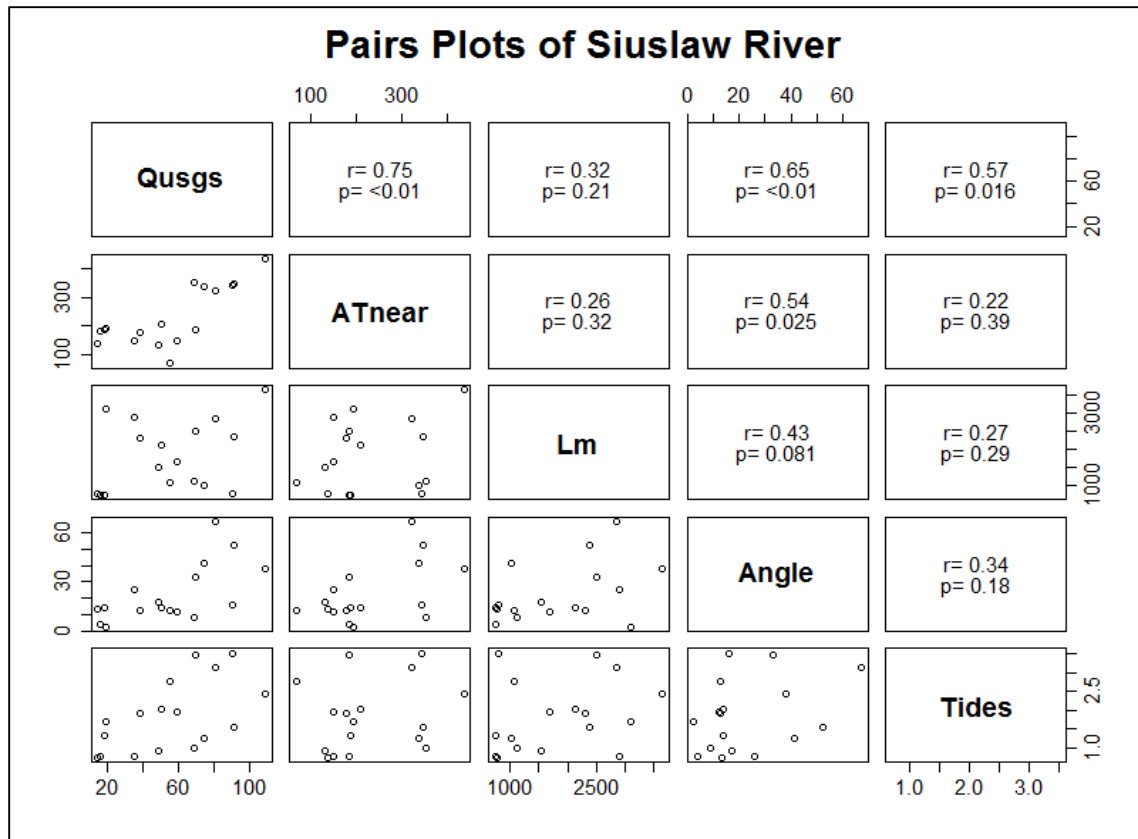


Figure-E. 1: Siuslaw River: Pair-wise scatter plots of predictors and independent variable (Q_{USGS}) with correlation (range: -1 to 1) and p-values with best correlation close to ± 1 for p-value < 0.1

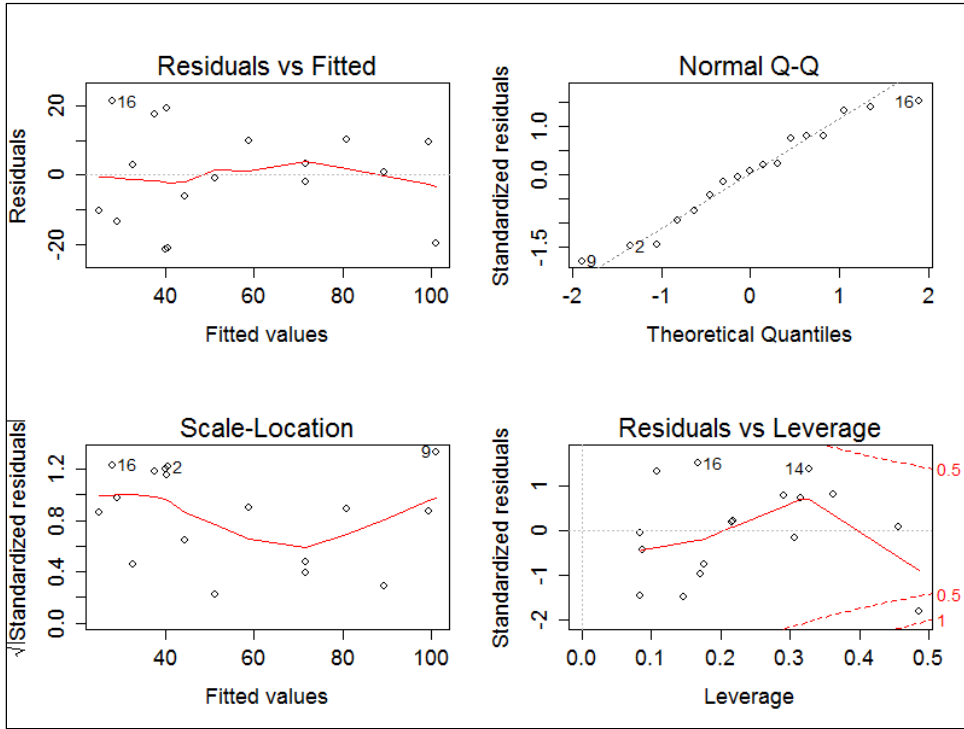


Figure-E. 2: Siuslaw River linear model diagnostic plots

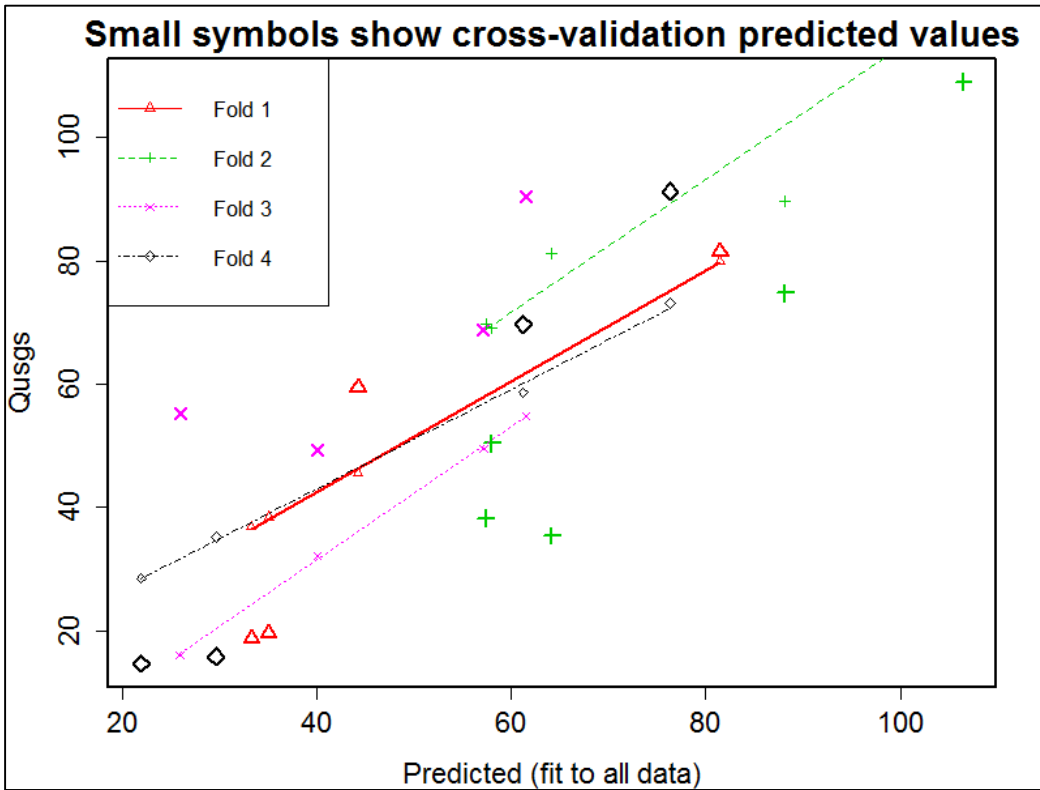


Figure-E. 3: Siuslaw River Cross Validation-Overall Mean Square 296

VI. DYNAMIC CHARACTERISTICS OF THE PLUME

Chetco River Plume's Dynamics Results

No	Image Ref.	Q (m3/s)	Rd	Km	P	hb
1	LE70470311999353EDC00	61.16	20.379	3.926	2.548	0.295
2	LE70470311999337EDC00	159.7	25.906	3.088	6.654	0.476
3	LE70460311999362EDC00	24.92	16.282	4.913	1.038	0.188
4	LE70460312000029EDC00	95.15	22.760	3.515	3.965	0.367
5	LE0470312000068EDC00	65.13	20.702	3.864	2.714	0.304
6	LE70460312000093EDC00	22.65	17.380	4.603	0.944	0.150
7	LE70470312000340EDC01	21.10	15.618	5.122	0.879	0.173
8	LE70460312000365EDC00	39.64	18.286	4.375	1.652	0.237
9	LE70470312001006EDC01	22.65	15.898	5.032	0.944	0.179
10	LE70460312001015EDC00	28.32	16.811	4.759	1.180	0.200
11	LE0470312001022EDC00	20.95	15.591	5.131	0.873	0.172
12	LE70460312001031EDC00	31.15	17.216	4.647	1.298	0.210
13	LE0470312001038EDC00	26.22	16.490	4.851	1.093	0.193
14	LE70460312001127EDC00	16.56	16.072	4.978	0.690	0.128
15	LE70460312002162EDC00	7.25	13.073	6.119	0.302	0.085
16	LE70460312003005EDC00	235.00	28.532	2.804	9.792	0.577
17	LE70460312003037EDC00	68.53	20.967	3.816	2.855	0.312
18	LE70460312003053EDC00	90.61	22.483	3.558	3.775	0.358
19	LE70460312004040EDC01	79.29	21.746	3.679	3.304	0.335
20	LE70460312004072EDC02	45.31	18.907	4.231	1.888	0.254
21	LE70460312004088EDC02	108.17	23.501	3.404	4.507	0.392
22	LE70460312005042EDC00	24.07	16.141	4.956	1.003	0.185
23	LE70460312006365EDC00	116.10	23.921	3.344	4.838	0.406
24	LE70460312008051EDC00	67.96	20.923	3.823	2.832	0.310
25	LE0460312008115EDC00	84.67	24.167	3.310	3.528	0.290
26	LE70460312008339EDC00	21.24	15.644	5.114	0.885	0.174
27	LE0460312009069EDC00	63.15	20.543	3.894	2.631	0.299
28	LE0460312009325EDC00	66.83	22.779	3.512	2.785	0.258
29	LE70460312009341EDC01	19.82	15.376	5.203	0.826	0.168
30	LE0460312009357EDC00	120.63	24.151	3.313	5.026	0.414
31	LE70460312010040EDC03	80.70	21.842	3.663	3.363	0.338
32	LE0460312010072EDC00	50.97	19.471	4.109	2.124	0.269

River Mouth W	80	m
Coriolis force f	9.74E-05	s-1
"g"	9.81	m/s ²
ρ_{amb} (Winter)	1014	kg/m ³
ρ_{amb} (Spring)	1020	kg/m ³
ρ_0	1000	kg/m ³
ho	3	m
ut	0.1	m/s
Winter-g'	0.13734	m/s ²
Spring-g'	0.1962	m/s ²

Kelvin Number	Km
Deformation Radius	Rd
Tidal Index	P
Predicted plume's depth	hb

Chetco River Plume's Dynamics Results

No	Image Ref.	Q (m3/s)	Rd	Km	P	hb
33	LE70460312011027EDC00	56.63	19.991	4.002	2.360	0.283
34	LE70460312011347EDC00	25.48	16.373	4.886	1.062	0.190
35	LE70460312012046EDC00	35.40	17.775	4.501	1.475	0.224
36	LE70460312013016EDC00	38.23	18.120	4.415	1.593	0.233
37	LE70460312013032EDC00	51.00	19.474	4.108	2.125	0.269
38	LE70470312013039EDC00	56.63	19.991	4.002	2.360	0.283
39	LE70470312013055EDC00	26.34	16.509	4.846	1.098	0.193
40	LE0460312013112EDC00	32.85	19.073	4.194	1.369	0.181
41	LE0460312013288EDC00	14.3	15.493	5.164	0.596	0.119
42	LE70470312013327EDC00	14.16	15.455	5.176	0.590	0.119
43	LE70470312013343EDC00	18.97	15.208	5.260	0.790	0.164
44	LE70470312013359EDC00	12.17	13.611	5.878	0.507	0.131
45	LE0460312014019EDC00	24.07	16.141	4.956	1.003	0.185
46	LE70470312014026EDC00	14.6	14.245	5.616	0.608	0.144
47	LE0460312014307EDC00	45.31	20.670	3.870	1.888	0.212
48	LE70470312014314EDC00	25.62	17.924	4.463	1.068	0.159
49	LE70470312014362ASN00	87.80	22.307	3.586	3.658	0.353
50	LE70470312015013EDC00	22.37	15.848	5.048	0.932	0.178
51	LE70470312015045EDC00	82.11	21.936	3.647	3.421	0.341
52	LE70460312015054EDC00	27.75	16.726	4.783	1.156	0.198
53	LE70470312015061EDC00	18.69	15.152	5.280	0.779	0.163
54	LE70460312015102EDC00	62.30	22.383	3.574	2.596	0.249
55	LE70470312015109EDC00	32.28	18.990	4.213	1.345	0.179
56	LE70470312015333EDC00	10.9	14.476	5.526	0.454	0.104

River Mouth W	80	m
Coriolis force f	9.74E-05	s-1
"g"	9.81	m/s ²
ρ_{amb} (Winter)	1014	kg/m ³
ρ_{amb} (Spring)	1020	kg/m ³
ρ_0	1000	kg/m ³
ho	3	m
ut	0.1	m/s
Winter-g'	0.13734	m/s ²
Spring-g'	0.1962	m/s ²

Kelvin Number	Km
Deformation Radius	Rd
Tidal Index	P
Predicted plume's depth	hb

Coquille River Plume's Dynamics Results

No	Image Ref.	Q (m3/s)	Rd	Km	P	hb
1	LE70470301999353EDC00	28.88	16.893	36.109	0.158	0.202
2	LE70460302000029PAC02	31.15	17.216	35.432	0.170	0.210
3	LE70460302000173EDC00	3.50	10.897	55.978	0.019	0.059
4	LE70460302001015EDC00	12.35	13.661	44.653	0.067	0.132
5	LE70470302001150EDC00	3.25	10.697	57.025	0.018	0.057
6	LE70470302002153EDC00	2.40	9.916	61.515	0.013	0.049
7	LE70460302003037EDC00	22.37	15.848	38.490	0.122	0.178
8	LE70460302004120EDC00	13.51	13.971	43.662	0.074	0.138
9	LE70470302005033EDC00	14.30	14.171	43.046	0.078	0.142
10	LE70470302006052EDC00	8.80	12.551	48.601	0.048	0.112
11	LE70460302006109EDC00	31.15	18.822	32.410	0.170	0.176
12	LE70460302007064EDC00	54.93	19.839	30.748	0.300	0.279
13	LE70460302007144EDC00	4.50	11.604	52.570	0.025	0.067
14	LE70470302009332EDC00	35.11	17.739	34.388	0.192	0.223
15	LE70460302009341EDC00	5.35	11.083	55.039	0.029	0.087
16	LE70460302009357EDC00	38.79	18.186	33.542	0.212	0.235
17	LE70460302010040EDC00	24.10	16.146	37.780	0.132	0.185
18	LE70470302010127EDC00	21.12	17.079	35.716	0.115	0.145
19	LE70470302011002EDC00	35.96	17.845	34.183	0.197	0.226
20	LE70470302011034EDC00	6.23	11.513	52.984	0.034	0.094
21	LE70470302011130EDC00	13.25	15.200	40.131	0.072	0.115
22	LE70470302011306EDC00	11.28	13.355	45.676	0.062	0.126
23	LE70460302011315EDC00	21.18	15.633	39.019	0.116	0.173
24	LE70460302003037EDC00	21.72	15.732	38.775	0.119	0.176
25	LE70470302012133EDC00	11.38	14.633	41.687	0.062	0.106
26	LE70460302013016EDC00	17.75	14.958	40.782	0.097	0.159
27	LE70470302013055EDC00	17.87	14.983	40.713	0.098	0.159
28	LE70470302013151EDC00	5.44	12.167	50.135	0.030	0.073
29	LE70470302013327EDC00	11.16	13.319	45.798	0.061	0.126
30	LE70470302013343EDC00	3.88	10.228	59.642	0.021	0.074
31	LE70460302014099EDC00	13.65	15.314	39.834	0.075	0.116
32	LE70470302015013EDC00	7.16	11.921	51.172	0.039	0.101

River Mouth W	610	m
Coriolis force f	9.74E-05	s-1
"g"	9.81	m/s ²
ρ_{amb} (Winter)	1014	kg/m ³
ρ_{amb} (Spring)	1020	kg/m ³
ρ_0	1000	kg/m ³
ho	3	m
ut	0.1	m/s
Winter-g'	0.13734	m/s ²
Spring-g'	0.1962	m/s ²

Kelvin Number	Km
Deformation Radius	Rd
Tidal Index	P
Predicted plume's depth	hb

Coquille River Plume's Dynamics Results

No	Image Ref.	Q (m ³ /s)	Rd	Km	P	hb
33	LE70470302015045EDC00	25.34	16.350	37.309	0.138	0.190
34	LE70470302015173EDC00	1.41	8.682	70.264	0.008	0.037
35	LE70470302015349EDC00	76.17	21.528	28.335	0.416	0.329
36	LE70470302015365EDC00	28.88	16.893	36.109	0.158	0.202

River Mouth W	610	m
Coriolis force f	9.74E-05	s-1
"g"	9.81	m/s ²
ρ_{amb} (Winter)	1014	kg/m ³
ρ_{amb} (Spring)	1020	kg/m ³
ρ_0	1000	kg/m ³
ho	3	m
ut	0.1	m/s
Winter-g'	0.13734	m/s ²
Spring-g'	0.1962	m/s ²

Kelvin Number	Km
Deformation Radius	Rd
Tidal Index	P
Predicted plume's depth	hb

Rogue River Plume's Dynamics Results

No	Image Ref.	Q (m3/s)	Rd	Km	P	hb
1	LE70470311999353EDC00	222.0	28.129	10.132	2.226	0.561
2	LE70470311999337EDC00	190.6	27.076	10.526	1.910	0.520
3	LE70460311999362EDC00	77.9	21.648	13.165	0.781	0.332
4	LE70460312000029EDC00	230.5	28.394	10.037	2.311	0.572
5	LE70470312000068EDC00	233.9	28.499	10.001	2.345	0.576
6	LE70460312000093EDC00	122.3	26.496	10.756	1.226	0.349
7	LE70470312000340EDC01	59.2	20.212	14.100	0.593	0.290
8	LE70460312000365EDC00	62.6	20.496	13.905	0.627	0.298
9	LE70470312001006EDC01	51.8	19.552	14.577	0.519	0.271
10	LE70460312001015EDC00	57.2	20.041	14.221	0.573	0.285
11	LE70460312001031EDC00	51.3	19.498	14.617	0.514	0.270
12	LE70470312001038EDC00	50.7	19.444	14.657	0.508	0.268
13	LE70460312001111EDC00	72.8	23.269	12.248	0.730	0.269
14	LE70470312001150EDC00	88.3	24.425	11.668	0.886	0.296
15	LE70460312002162EDC00	104.5	25.472	11.189	1.048	0.322
16	LE70460312003005EDC00	299.3	30.311	9.403	3.001	0.652
17	LE70460312003037EDC00	176.7	26.569	10.727	1.771	0.501
18	LE70460312003053EDC00	182.4	26.779	10.643	1.828	0.509
19	LE70460312004040EDC01	168.8	26.266	10.851	1.692	0.489
20	LE70460312004088EDC02	186.6	26.934	10.581	1.871	0.514
21	LE70460312004120EDC02	123.2	26.542	10.738	1.235	0.350
22	LE70460312005042EDC00	68.8	20.988	13.579	0.690	0.312
23	LE70460312006109EDC00	246.9	31.581	9.024	2.475	0.495
24	LE70460312006285EDC00	40.2	20.062	14.206	0.403	0.200
25	LE70460312006365EDC00	314.3	30.684	9.288	3.151	0.668
26	LE70460312008051EDC00	197.1	27.304	10.438	1.976	0.529
27	LE70460312008115EDC00	170.8	28.799	9.896	1.712	0.412
28	LE70460312008339EDC00	54.7	19.814	14.384	0.548	0.278
29	LE70460312009341EDC01	54.7	19.814	14.384	0.548	0.278
30	LE70460312009357EDC00	125.2	24.374	11.693	1.255	0.421
31	LE70460312010040EDC03	125.7	24.402	11.679	1.260	0.422
32	LE70460312010072EDC00	215.8	27.930	10.204	2.163	0.553

River Mouth W	285	m
Coriolis force f	9.74E-05	s-1
" g "	9.81	m/s ²
ρ_{amb} (Winter)	1014	kg/m ³
ρ_{amb} (Spring)	1020	kg/m ³
ρ_0	1000	kg/m ³
h_0	3.5	m
u_t	0.1	m/s
Winter- g'	0.13734	m/s ²
Spring- g'	0.1962	m/s ²

Kelvin Number	Km
Deformation Radius	Rd
Tidal Index	P
Predicted plume's depth	hb

Rogue River Plume's Dynamics Results

No	Image Ref.	Q (m3/s)	Rd	Km	P	hb
33	LE70460312011027EDC00	261.1	29.293	9.729	2.617	0.609
34	LE70460312011123EDC00	217.8	30.604	9.312	2.183	0.465
35	LE70460312011347EDC00	64.6	20.657	13.797	0.647	0.303
36	LE70460312012046EDC00	117.2	23.979	11.885	1.175	0.408
37	LE70460312012062EDC00	179.5	26.675	10.684	1.800	0.505
38	LE70460312013016EDC00	149.2	25.470	11.190	1.496	0.460
39	LE70460312013032EDC00	238.4	28.636	9.953	2.390	0.582
40	LE70470312013039EDC00	181.5	26.748	10.655	1.820	0.507
41	LE70470312013055EDC00	119.8	24.108	11.822	1.201	0.412
42	LE70460312013112EDC00	119.8	26.357	10.813	1.201	0.345
43	LE70460312013288EDC00	56.4	21.828	13.057	0.565	0.237
44	LE70470312013327EDC00	66.8	20.836	13.679	0.670	0.308
45	LE70470312013343EDC00	52.1	19.579	14.557	0.522	0.272
46	LE70470312013359EDC00	56.4	19.966	14.274	0.565	0.283
47	LE70470312014026EDC00	45.9	18.965	15.028	0.460	0.255
48	LE70460312014147EDC00	75.0	23.448	12.154	0.752	0.273
49	LE70460312014275EDC00	43.3	20.440	13.943	0.434	0.207
50	LE70470312014314EDC00	54.9	19.839	14.365	0.551	0.279
51	LE70470312014362ASN00	325.6	30.957	9.206	3.265	0.680
52	LE70470312015013EDC00	107.6	23.471	12.143	1.079	0.391
53	LE70470312015045EDC00	258.8	29.229	9.751	2.595	0.606
54	LE70460312015054EDC00	108.5	23.517	12.119	1.087	0.392
55	LE70470312015061EDC00	92.0	22.571	12.627	0.923	0.361
56	LE70460312015102EDC00	83.0	24.045	11.853	0.832	0.287
57	LE70470312015109EDC00	73.1	23.292	12.236	0.732	0.269

River Mouth W	285	m
Coriolis force f	9.74E-05	s-1
"g"	9.81	m/s ²
ρ_{amb} (Winter)	1014	kg/m ³
ρ_{amb} (Spring)	1020	kg/m ³
ρ_0	1000	kg/m ³
ho	3.5	m
ut	0.1	m/s
Winter-g'	0.13734	m/s ²
Spring-g'	0.1962	m/s ²

Kelvin Number	Km
Deformation Radius	Rd
Tidal Index	P
Predicted plume's depth	hb

Siuslaw River Plume's Dynamics Results

No	Image Ref.	Q (m3/s)	Rd	Km	P	hb
1	LE70460302000029PAC02	68.81	20.988	9.529	0.983	0.312
2	LE70460302000173EDC00	19.54	16.750	11.940	0.279	0.139
3	LE70460302001015EDC00	74.76	21.428	9.334	1.068	0.326
4	LE70470292001150EDC00	35.40	19.433	10.292	0.506	0.187
5	LE70470292002137EDC00	18.69	16.565	12.074	0.267	0.136
6	LE70470292002153EDC00	14.67	15.591	12.828	0.210	0.121
7	LE70460302003037EDC00	90.33	22.466	8.902	1.290	0.358
8	LE70460302004120EDC00	38.23	19.810	10.096	0.546	0.195
9	LE70470292005033EDC00	81.42	21.890	9.137	1.163	0.340
10	LE70460302005330EDC00	91.18	22.519	8.882	1.303	0.360
11	LE70460302006109EDC00	69.66	23.016	8.689	0.995	0.263
12	LE70460302007144EDC00	15.80	15.884	12.591	0.226	0.125
13	LE70460302009357EDC00	109.02	23.547	8.493	1.557	0.393
14	LE70460302011027EDC00	55.22	19.865	10.068	0.789	0.280
15	LE70460302011046EDC00	50.40	19.417	10.300	0.720	0.267
16	LE70460302013016EDC00	49.27	19.307	10.359	0.704	0.264
17	LE70460302013032EDC00	59.47	20.236	9.883	0.850	0.290

River Mouth W	200	m
Coriolis force f	9.74E-05	s-1
"g"	9.81	m/s ²
ρ_{amb} (Winter)	1014	kg/m ³
ρ_{amb} (Spring)	1020	kg/m ³
ρ_0	1000	kg/m ³
ho	3.5	m
ut	0.1	m/s
Winter-g'	0.13734	m/s ²
Spring-g'	0.1962	m/s ²

Kelvin Number	Km
Deformation Radius	Rd
Tidal Index	P
Predicted plume's depth	hb

VII. Contingency tables for the assessment of the “ENVI” extraction method

Confusion matrices for the assessment of the classification method in ENVI (Chetco River)

Image Number	Date	Q(m3/s)	A_1	A_2	A_3	A_4	A_Tot	Man A_Tot	TP	FP	FN	TN	TPR	F	BIAS	HSS
LE70470311999353EDC00	19.03.1999	61.16	230				230	224	204	26	20	4750	0.911	0.899	1.027	0.894
LE70470311999337EDC00	03.12.1999	159.7	470	561	800		1831	1885	1752	79	133	3036	0.929	0.943	0.971	0.909
LE70460311999362EDC00	28.12.1999	24.92	323				323	342	299	24	43	4634	0.874	0.899	0.944	0.892
LE70460312000029EDC00	29.01.2000	95.15	273				273	292	251	22	41	4686	0.860	0.888	0.935	0.882
LE0470312000068EDC00	08.03.2000	65.13	452				452	476	411	41	65	4483	0.863	0.886	0.950	0.874
LE70460312000093EDC00	02.04.2000	22.65	124	174			298	306	279	19	27	4675	0.912	0.924	0.974	0.919
LE70470312000340EDC01	05.12.2000	21.10	223	508			731	715	686	45	29	4240	0.959	0.949	1.022	0.940
LE70460312000365EDC00	30.12.2000	39.64	303	511			814	777	747	67	30	4156	0.961	0.939	1.048	0.928
LE70470312001006EDC01	06.01.2001	22.65	77	141	304	466	988	995	957	31	38	3974	0.962	0.965	0.993	0.957
LE70460312001015EDC00	15.01.2001	28.32	75	181	311		567	546	519	48	27	4406	0.951	0.933	1.038	0.924
LE0470312001022EDC00	22.01.2001	20.95	89	176			265	259	239	26	20	4715	0.923	0.912	1.023	0.907
LE70460312001031EDC00	31.01.2001	31.15	132	201	582		915	944	881	34	63	4022	0.933	0.948	0.969	0.936
LE0470312001038EDC00	07.02.2001	26.22	76	194			270	288	256	14	32	4698	0.889	0.918	0.938	0.913
LE70460312001127EDC00	07.05.2001	16.56	23	69			92	100	80	12	20	4888	0.800	0.833	0.920	0.830
LE70460312002162EDC00	11.06.2002	7.25	83				83	73	64	19	9	4908	0.877	0.821	1.137	0.818
LE70460312003005EDC00	05.01.2003	235.00	3338				3338	3416	3211	127	205	1457	0.940	0.951	0.977	0.849
LE70460312003037EDC00	06.02.2003	68.53	96	171	485		752	789	728	24	61	4187	0.923	0.945	0.953	0.935
LE70460312003053EDC00	22.02.2003	90.61	665				665	662	638	27	24	4311	0.964	0.962	1.005	0.956
LE70460312004040EDC01	09.02.2004	79.29	81	212	340		633	614	592	41	22	4345	0.964	0.949	1.031	0.942
LE70460312004072EDC02	12.03.2004	45.31	151				151	146	134	17	12	4837	0.918	0.902	1.034	0.899
LE70460312004088EDC02	28.03.2004	108.17	839				839	816	777	62	39	4122	0.952	0.939	1.028	0.927
LE70460312005042EDC00	11.02.2005	24.07	64	216	382		662	636	611	51	25	4313	0.961	0.941	1.041	0.933
LE70460312006365EDC00	31.12.2006	116.10	631				631	644	602	29	42	4327	0.935	0.944	0.980	0.936
LE70460312008051EDC00	20.02.2008	67.96	225				225	220	204	21	16	4759	0.927	0.917	1.023	0.913
LE0460312008115EDC00	24.04.2008	84.67	887				887	884	854	33	30	4083	0.966	0.964	1.003	0.957
LE70460312008339EDC00	04.12.2008	21.24	629				629	646	604	25	42	4329	0.935	0.947	0.974	0.940
LE0460312009069EDC00	10.03.2009	63.15	436				436	429	403	33	26	4538	0.939	0.932	1.016	0.925
LE0460312009325EDC00	21.11.2009	66.83	368				368	365	335	33	30	4602	0.918	0.914	1.008	0.907
LE70460312009341EDC01	07.12.2009	19.82	129	101	224	393	847	824	798	49	26	4127	0.968	0.955	1.028	0.946
LE0460312009357EDC00	23.12.2009	120.63	303	426	500		1229	1225	1184	45	41	3730	0.967	0.965	1.003	0.954
LE70460312010040EDC03	09.02.2010	80.70	177	1214			1391	1414	1334	57	80	3529	0.943	0.951	0.984	0.932
LE0460312010072EDC00	13.03.2010	50.97	361				361	344	315	46	29	4610	0.916	0.894	1.049	0.886
LE70460312011027EDC00	27.01.2011	56.63	180				180	190	171	9	19	4801	0.900	0.924	0.947	0.921
LE70460312011347EDC00	13.12.2011	25.48	30	59	120		209	216	190	19	26	4765	0.880	0.894	0.968	0.889
LE70460312012046EDC00	15.02.2012	35.40	119	388			507	499	457	50	42	4451	0.916	0.909	1.016	0.898
LE70460312013016EDC00	16.01.2013	38.23	133	134	178	446	891	882	851	40	31	4078	0.965	0.960	1.010	0.951

Confusion matrices for the assessment of the classification method in ENVI (Chetco River)

Image Number	Date	Q(m3/s)	A_1	A_2	A_3	A_4	A_Tot	Man A_Tot	TP	FP	FN	TN	TPR	F	BIAS	HSS
LE70460312013032EDC00	01.02.2013	51.00	105	435	554		1094	1041	998	96	43	3863	0.959	0.935	1.051	0.917
LE70470312013039EDC00	08.02.2013	56.63	310				310	309	285	25	24	4666	0.922	0.921	1.003	0.916
LE70470312013055EDC00	24.02.2013	26.34	406				406	410	377	29	33	4561	0.920	0.924	0.990	0.917
LE0460312013112EDC00	22.04.2013	32.85	45	68	95		208	197	184	24	13	4779	0.934	0.909	1.056	0.905
LE0460312013288EDC00	15.10.2013	14.3	76				76	74	65	11	9	4915	0.878	0.867	1.027	0.865
LE70470312013327EDC00	23.11.2013	14.16	36				36	33	29	7	4	4960	0.879	0.841	1.091	0.839
LE70470312013343EDC00	09.12.2013	18.97	23	43	65		131	125	118	13	7	4862	0.944	0.922	1.048	0.920
LE70470312013359EDC00	25.12.2013	12.17	218				218	206	192	26	14	4768	0.932	0.906	1.058	0.901
LE0460312014019EDC00	19.01.2014	24.07	95				95	95	85	10	10	4895	0.895	0.895	1.000	0.893
LE70470312014026EDC00	26.01.2014	14.6	216				216	227	195	21	32	4752	0.859	0.880	0.952	0.875
LE0460312014307EDC00	03.11.2014	45.31	479				479	465	432	47	33	4488	0.929	0.915	1.030	0.906
LE70470312014314EDC00	10.11.2014	25.62	35	80	265		380	406	358	22	48	4572	0.882	0.911	0.936	0.903
LE70470312014362ASN00	28.12.2014	87.80	271	673			944	984	906	38	78	3978	0.921	0.940	0.959	0.925
LE70470312015013EDC00	13.01.2015	22.37	122				122	127	115	7	12	4866	0.906	0.924	0.961	0.922
LE70470312015045EDC00	14.02.2015	82.11	274	747			1021	1068	973	48	95	3884	0.911	0.932	0.956	0.913
LE70460312015054EDC00	23.02.2015	27.75	154	709			863	852	811	52	41	4096	0.952	0.946	1.013	0.935
LE70470312015061EDC00	02.03.2015	18.69	63				63	58	52	11	6	4931	0.897	0.860	1.086	0.858
LE70460312015102EDC00	12.04.2015	62.30	856				856	853	814	42	39	4105	0.954	0.953	1.004	0.943
LE70470312015109EDC00	19.04.2015	32.28	362				362	365	336	26	29	4609	0.921	0.924	0.992	0.918
LE70470312015333EDC00	29.11.2015	10.9	14	45	76		135	134	127	8	7	4858	0.948	0.944	1.007	0.943

Legend:

- A_1 Area of Temperature T1 of the plume measured by ENVI
- A_2 Area of Temperature T2 of the plume measured by ENVI
- A_3 Area of Temperature T3 of the plume measured by ENVI
- A_4 Area of Temperature T4 of the plume measured by ENVI
- A_Tot Summation of the total area of the plume measured by ENVI
- Man_A_Tot Summation of the total area of the plume measured manually
- TP (True Positive) It report the intersection area in number of pixels between both extraction methods
- FP (False Positive) It represents the part of the "ENVI" plume that did not overlap an area of the "Manually" plume
- FN (False Negative) It represents the part of the "Manually" plume that was missed by the "ENVI" plume
- TN (True Negative) It represents the area outside both the "Manually" and the "ENVI" plume regions

Average	0.922	0.921	1.003	0.911
Minimum	0.800	0.821	0.920	0.818
Maximum	0.968	0.965	1.137	0.957
Std Dev	0.035	0.033	0.043	0.032

Confusion matrices for the assessment of the classification method in ENVI (Coquille River)

Image Number	Date	Q(m3/s)	A_1	A_2	A_3	A_4	A_Tot	Man A_Tot	TP	FP	FN	TN	TPR	F	BIAS	HSS
LE/0470301999353EDC00	19.12.1999	28.88	463				463	440	417	46	23	6514	0.948	0.924	1.052	0.918
LE70460302000029PAC02	29.01.2000	31.15	144	197	152		493	471	438	55	33	6474	0.930	0.909	1.047	0.902
LE70460302000173EDC00	21.06.2000	3.50	64	91	129		284	285	258	26	27	6689	0.905	0.907	0.996	0.903
LE70460302001015EDC00	15.01.2001	12.35	469				469	465	438	31	27	6504	0.942	0.938	1.009	0.933
LE70470302001150EDC00	30.05.2001	3.25	92	183			275	281	249	26	32	6693	0.886	0.896	0.979	0.891
LE70470302002153EDC00	02.06.2002	2.40	236				236	234	220	16	14	6750	0.940	0.936	1.009	0.934
LE70460302003037EDC00	06.02.2003	22.37	162				162	151	136	26	15	6823	0.901	0.869	1.073	0.866
LE70460302004120EDC00	29.04.2004	13.51	44	76	111		231	216	205	26	11	6758	0.949	0.917	1.069	0.914
LE70470302005033EDC00	02.02.2005	14.30	377				377	372	352	25	20	6603	0.946	0.940	1.013	0.937
LE70470302006052EDC00	21.02.2006	8.80	272				272	281	245	27	36	6692	0.872	0.886	0.968	0.881
LE70460302006109EDC00	19.04.2006	31.15	300				300	279	260	40	19	6681	0.932	0.898	1.075	0.894
LE70460302007064EDC00	05.03.2007	54.93	453				453	483	416	37	67	6480	0.861	0.889	0.938	0.881
LE70460302007144EDC00	24.05.2007	4.50	47	53	73		173	165	153	20	12	6815	0.927	0.905	1.048	0.903
LE70470302009332EDC00	28.11.2009	35.11	160	326			486	518	455	31	63	6451	0.878	0.906	0.938	0.899
LE70460302009341EDC00	07.12.2009	5.35	68				68	59	52	16	7	6925	0.881	0.819	1.153	0.817
LE70460302009357EDC00	23.12.2009	38.79	76	104			180	174	159	21	15	6805	0.914	0.898	1.034	0.896
LE70460302010040EDC00	09.02.2010	24.10	268				268	256	242	26	14	6718	0.945	0.924	1.047	0.921
LE70470302010127EDC00	07.05.2010	21.12	140	170			310	289	264	46	25	6665	0.913	0.881	1.073	0.876
LE70470302011002EDC00	02.01.2011	35.96	156	269			425	407	369	56	38	6537	0.907	0.887	1.044	0.880
LE70470302011034EDC00	03.02.2011	6.23	100				100	98	86	14	12	6888	0.878	0.869	1.020	0.867
LE70470302011130EDC00	10.05.2011	13.25	73	140			213	219	201	12	18	6769	0.918	0.931	0.973	0.928
LE70470302011306EDC00	02.11.2011	11.28	30	150			180	188	169	11	19	6801	0.899	0.918	0.957	0.916
LE70460302011315EDC00	11.11.2011	21.18	210				210	224	191	19	33	6757	0.853	0.880	0.938	0.876
LE70460302003037EDC00	15.02.2012	21.72	230				230	224	208	22	16	6754	0.929	0.916	1.027	0.913
LE70470302012133EDC00	12.05.2012	11.38	43	105			148	154	134	14	20	6832	0.870	0.887	0.961	0.885
LE70460302013016EDC00	16.01.2013	17.75	187				187	191	170	17	21	6792	0.890	0.899	0.979	0.897

Confusion matrices for the assessment of the classification method in ENVI (Coquille River)

Image Number	Date	Q(m3/s)	A_1	A_2	A_3	A_4	A_Tot	Man A_Tot	TP	FP	FN	TN	TPR	F	BIAS	HSS
LE70470302013055EDC00	24.02.2013	17.87	195				195	202	183	12	19	6786	0.906	0.922	0.965	0.920
LE70470302013151EDC00	31.05.2013	5.44	75	90			165	165	153	12	12	6823	0.927	0.927	1.000	0.926
LE70470302013327EDC00	23.11.2013	11.16	165				165	167	149	16	18	6817	0.892	0.898	0.988	0.895
LE70470302013343EDC00	09.12.2013	3.88	86				86	96	76	10	20	6894	0.792	0.835	0.896	0.833
LE70460302014099EDC00	09.04.2014	13.65	84	102			186	176	159	27	17	6797	0.903	0.878	1.057	0.875
LE70470302015013EDC00	13.01.2015	7.16	109				109	103	95	14	8	6883	0.922	0.896	1.058	0.895
LE70470302015045EDC00	14.02.2015	25.34	316				316	300	284	32	16	6668	0.947	0.922	1.053	0.918
LE70470302015173EDC00	22.06.2015	1.41	46	58			104	107	98	6	9	6887	0.916	0.929	0.972	0.928
LE70470302015349EDC00	15.12.2015	76.17	432				432	425	400	32	25	6543	0.941	0.933	1.016	0.929
LE70470302015365EDC00	31.12.2015	28.88	324				324	330	299	25	31	6645	0.906	0.914	0.982	0.910

Legend:

- A_1 Area of Temperature T1 of the plume measured by ENVI
- A_2 Area of Temperature T2 of the plume measured by ENVI
- A_3 Area of Temperature T3 of the plume measured by ENVI
- A_4 Area of Temperature T4 of the plume measured by ENVI
- A_Tot Summation of the total area of the plume measured by ENVI
- Man_A_Tot Summation of the total area of the plume measured manually
- TP (True Positive) It report the intersection area in number of pixels between both extraction methods
- FP (False Positive) It represents the part of the "ENVI" plume that did not overlap an area of the "Manually" plume
- FN (False Negative) It represents the part of the "Manually" plume that was missed by the "ENVI" plume
- TN (True Negative) It represents the area outside both the "Manually" and the "ENVI" plume regions

Average	0.907	0.902	1.011	0.899
Minimum	0.792	0.819	0.896	0.817
Maximum	0.949	0.940	1.153	0.937
Std Dev	0.03	0.03	0.05	0.03

Confusion matrices for the assessment of the classification method in ENVI (Rogue River)

Image Number	Date	Q(m3/s)	A_1	A_2	A_3	A_4	A_Tot	Man A_Tot	TP	FP	FN	TN	TPR	F	BIAS	HSS
LE70470311999353EDC00	19.03.1999	222.0	178				178	187	168	10	19	9803	0.898	0.921	0.952	0.919
LE70470311999337EDC00	03.12.1999	190.6	166				166	176	155	11	21	9813	0.881	0.906	0.943	0.905
LE70460311999362EDC00	28.12.1999	77.9	62				62	53	46	16	7	9931	0.868	0.800	1.170	0.799
LE70460312000029EDC00	29.01.2000	230.5	171				171	179	161	10	18	9811	0.899	0.920	0.955	0.919
LE70470312000068EDC00	08.03.2000	233.9	173				173	185	162	11	23	9804	0.876	0.905	0.935	0.903
LE70460312000093EDC00	02.04.2000	122.3	34				34	37	29	5	8	9958	0.784	0.817	0.919	0.816
LE70470312000340EDC01	05.12.2000	59.2	223	508			731	715	690	41	25	9244	0.965	0.954	1.022	0.951
LE70460312000365EDC00	30.12.2000	62.6	303	711			1014	1015	967	47	48	8938	0.953	0.953	0.999	0.948
LE70470312001006EDC01	06.01.2001	51.8	77	241	344	526	1188	1156	1117	71	39	8773	0.966	0.953	1.028	0.947
LE70460312001015EDC00	15.01.2001	57.2	75	181	311		567	545	521	46	24	9409	0.956	0.937	1.040	0.933
LE70460312001031EDC00	31.01.2001	51.3	132	201	582		915	884	852	63	32	9053	0.964	0.947	1.035	0.942
LE70470312001038EDC00	07.02.2001	50.7	22				22	23	19	3	4	9974	0.826	0.844	0.957	0.844
LE70460312001111EDC00	21.04.2001	72.8	36				36	36	32	4	4	9960	0.889	0.889	1.000	0.888
LE70470312001150EDC00	30.05.2001	88.3	43				43	39	35	8	4	9953	0.897	0.854	1.103	0.853
LE70460312002162EDC00	11.06.2002	104.5	63				63	58	51	12	7	9930	0.879	0.843	1.086	0.842
LE70460312003005EDC00	05.01.2003	299.3	254				254	259	235	19	24	9722	0.907	0.916	0.981	0.914
LE70460312003037EDC00	06.02.2003	176.7	96	171			267	252	229	38	23	9710	0.909	0.882	1.060	0.879
LE70460312003053EDC00	22.02.2003	182.4	155				155	161	144	11	17	9828	0.894	0.911	0.963	0.910
LE70460312004040EDC01	09.02.2004	168.8	81	312			393	383	356	37	27	9580	0.930	0.918	1.026	0.914
LE70460312004088EDC02	28.03.2004	186.6	149				149	156	140	9	16	9835	0.897	0.918	0.955	0.917
LE70460312004120EDC02	29.04.2004	123.2	156				156	161	143	13	18	9826	0.888	0.902	0.969	0.901
LE70460312005042EDC00	11.02.2005	68.8	64	216			280	264	244	36	20	9700	0.924	0.897	1.061	0.894
LE70460312006109EDC00	19.04.2006	246.9	142	226			368	346	313	55	33	9599	0.905	0.877	1.064	0.872
LE70460312006285EDC00	12.10.2006	40.2	22				22	22	19	3	3	9975	0.864	0.864	1.000	0.863
LE70460312006365EDC00	31.12.2006	314.3	239				239	254	226	13	28	9733	0.890	0.917	0.941	0.915
LE70460312008051EDC00	20.02.2008	197.1	225	1616			1841	1898	1764	77	134	8025	0.929	0.944	0.970	0.931
LE70460312008115EDC00	24.04.2008	170.8	147				147	145	131	16	14	9839	0.903	0.897	1.014	0.896
LE70460312008339EDC00	04.12.2008	54.7	46				46	49	41	5	8	9946	0.837	0.863	0.939	0.863
LE70460312009341EDC01	07.12.2009	54.7	35	121			156	162	141	15	21	9823	0.870	0.887	0.963	0.885
LE70460312009357EDC00	23.12.2009	125.2	81				81	77	68	13	9	9910	0.883	0.861	1.052	0.860
LE70460312010040EDC03	09.02.2010	125.7	146	1197			1343	1340	1281	62	59	8598	0.956	0.955	1.002	0.948
LE70460312010072EDC00	13.03.2010	215.8	154				154	160	145	9	15	9831	0.906	0.924	0.963	0.922
LE70460312011027EDC00	27.01.2011	261.1	180	2414			2594	2633	2485	109	148	7258	0.944	0.951	0.985	0.933
LE70460312011123EDC00	03.05.2011	217.8	115	256			371	376	345	26	31	9598	0.918	0.924	0.987	0.921

Confusion matrices for the assessment of the classification method in ENVI (Rogue River)

Image Number	Date	Q(m3/s)	A_1	A_2	A_3	A_4	A_Tot	Man A_Tot	TP	FP	FN	TN	TPR	F	BIAS	HSS
LE70460312011347EDC00	13.12.2011	64.6	30	59	120		209	211	193	16	18	9773	0.915	0.919	0.991	0.917
LE70460312012046EDC00	15.02.2012	117.2	119	388			507	510	487	20	23	9470	0.955	0.958	0.994	0.955
LE70460312012062EDC00	02.03.2012	179.5	143				143	149	131	12	18	9839	0.879	0.897	0.960	0.896
LE70460312013016EDC00	16.01.2013	149.2	133	134	178		445	431	401	44	30	9525	0.930	0.916	1.032	0.912
LE70460312013032EDC00	01.02.2013	238.4	105	435			540	558	518	22	40	9420	0.928	0.944	0.968	0.940
LE70470312013039EDC00	08.02.2013	181.5	134				134	140	127	7	13	9853	0.907	0.927	0.957	0.926
LE70470312013055EDC00	24.02.2013	119.8	132				132	139	122	10	17	9851	0.878	0.900	0.950	0.899
LE70460312013112EDC00	22.04.2013	119.8	78				78	78	69	9	9	9913	0.885	0.885	1.000	0.884
LE70460312013288EDC00	15.10.2013	56.4	30				30	32	27	3	5	9965	0.844	0.871	0.938	0.871
LE70470312013327EDC00	23.11.2013	66.8	49				49	49	42	7	7	9944	0.857	0.857	1.000	0.856
LE70470312013343EDC00	09.12.2013	52.1	38				38	38	33	5	5	9957	0.868	0.868	1.000	0.868
LE70470312013359EDC00	25.12.2013	56.4	49				49	50	43	6	7	9944	0.860	0.869	0.980	0.868
LE70470312014026EDC00	26.01.2014	45.9	37				37	42	33	4	9	9954	0.786	0.835	0.881	0.835
LE70460312014147EDC00	27.05.2014	75.0	41				41	44	35	6	9	9950	0.795	0.824	0.932	0.823
LE70460312014275EDC00	02.10.2014	43.3	40				40	43	35	5	8	9952	0.814	0.843	0.930	0.843
LE70470312014314EDC00	10.11.2014	54.9	35	80	265		380	369	337	43	32	9588	0.913	0.900	1.030	0.896
LE70470312014362ASN00	28.12.2014	325.6	271	1473			1744	1796	1662	82	134	8122	0.925	0.939	0.971	0.926
LE70470312015013EDC00	13.01.2015	107.6	81				81	73	63	18	10	9909	0.863	0.818	1.110	0.817
LE70470312015045EDC00	14.02.2015	258.8	274	1347			1621	1644	1551	70	93	8286	0.943	0.950	0.986	0.940
LE70460312015054EDC00	23.02.2015	108.5	154	709			863	837	799	64	38	9099	0.955	0.940	1.031	0.934
LE70470312015061EDC00	02.03.2015	92.0	73				73	74	65	8	9	9918	0.878	0.884	0.986	0.883
LE70460312015102EDC00	12.04.2015	83.0	50				50	53	44	6	9	9941	0.830	0.854	0.943	0.854
LE70470312015109EDC00	19.04.2015	73.1	34				34	33	29	5	4	9962	0.879	0.866	1.030	0.865

Legend:

- A_1 Area of Temperature T1 of the plume measured by ENVI
- A_2 Area of Temperature T2 of the plume measured by ENVI
- A_3 Area of Temperature T3 of the plume measured by ENVI
- A_4 Area of Temperature T4 of the plume measured by ENVI
- A_Tot Summation of the total area of the plume measured by ENVI
- Man_A_Tot Summation of the total area of the plume measured manually
- TP (True Positive) It report the intersection area in number of pixels between both extraction methods
- FP (False Positive) It represents the part of the "ENVI" plume that did not overlap an area of the "Manually" plume
- FN (False Negative) It represents the part of the "Manually" plume that was missed by the "ENVI" plume

Average	0.894	0.896	0.994	0.893
Minimum	0.784	0.800	0.881	0.799
Maximum	0.966	0.958	1.170	0.955
Std Dev	0.045	0.041	0.053	0.039

Confusion matrices for the assessment of the classification method in ENVI (Siuslaw River)

Image Number	Date	Q(m3/s)	A_1	A_2	A_3	A_4	A_Tot	Man A_Tot	TP	FP	FN	TN	TPR	F	BIAS	HSS
LE70460302000029PAC02	01.29.00	68.81	131	222			353	368	330	23	38	609	0.897	0.915	0.959	0.868
LE70460302000173EDC00	06.21.00	19.54	194				194	200	181	13	19	787	0.905	0.919	0.970	0.899
LE70460302001015EDC00	01.15.01	74.76	646				646	639	617	29	22	332	0.966	0.960	1.011	0.889
LE70470292001150EDC00	05.30.01	35.40	151				151	156	139	12	17	832	0.891	0.906	0.968	0.888
LE70470292002137EDC00	05.17.02	18.69	64	123			187	186	171	16	15	798	0.919	0.917	1.005	0.898
LE70470292002153EDC00	06.02.02	14.67	138				138	142	129	9	13	849	0.908	0.921	0.972	0.909
LE70460302003037EDC00	02.06.03	90.33	113	231			344	358	326	18	32	624	0.911	0.929	0.961	0.890
LE70460302004120EDC00	04.29.04	38.23	42	136			178	183	166	12	17	805	0.907	0.920	0.973	0.902
LE70470292005033EDC00	02.02.05	81.42	203	118			321	339	304	17	35	644	0.897	0.921	0.947	0.882
LE70460302005330EDC00	11.26.05	91.18	114	232			346	360	326	20	34	620	0.906	0.924	0.961	0.882
LE70460302006109EDC00	04.19.06	69.66	186				186	173	160	26	13	801	0.925	0.891	1.075	0.868
LE70460302007144EDC00	05.24.07	15.80	38	146			184	181	168	16	13	803	0.928	0.921	1.017	0.903
LE70460302009357EDC00	12.23.09	109.02	136	300			436	446	410	26	36	528	0.919	0.930	0.978	0.874
LE70460302011027EDC00	01.27.11	55.22	69				69	62	54	15	8	923	0.871	0.824	1.113	0.812
LE70460302011046EDC00	02.15.12	50.40	63	146			209	204	192	17	12	779	0.941	0.930	1.025	0.912
LE70460302013016EDC00	01.16.13	49.27	61	72			133	133	125	8	8	859	0.940	0.940	1.000	0.931
LE70460302013032EDC00	02.01.13	59.47	149				149	144	133	16	11	840	0.924	0.908	1.035	0.892

Legend:

- A_1 Area of Temperature T1 of the plume measured by ENVI
- A_2 Area of Temperature T2 of the plume measured by ENVI
- A_3 Area of Temperature T3 of the plume measured by ENVI
- A_4 Area of Temperature T4 of the plume measured by ENVI
- A_Tot Summation of the total area of the plume measured by ENVI
- Man_A_Tot Summation of the total area of the plume measured manually
- TP (True Positive) It report the intersection area in number of pixels between both extraction methods
- FP (False Positive) It represents the part of the "ENVI" plume that did not overlap an area of the "Manually" plume
- FN (False Negative) It represents the part of the "Manually" plume that was missed by the "ENVI" plume
- TN (True Negative) It represents the area outside both the "Manually" and the "ENVI" plume regions

Average	0.915	0.916	0.998	0.888
Minimum	0.871	0.824	0.947	0.812
Maximum	0.966	0.960	1.113	0.931
Std dev	0.022	0.028	0.045	0.025

VIII. MATLAB CODE FOR ELLIPTICAL FIT FOR PLUME SHAPE

The files created in ENVI representing the plume area have the following formats: .shp, .dbf, .shx, .ebb. The “.shp” file is imported in the mapview and saved as an image file “.png”.

Here below we list the routine code written in Matlab and used to fit the ellipse of each plume’s area. Illustration of the overlap between the plume and ellipse areas, the fitting ellipse around the plume’s area are added and the accuracy rate and F1 score based on confusion matrix of the overlap are computed.

The created function “fit_ellipse_pca” based on the principal component analysis called in the routine is listed too.

```
%read the image file converted from the shp file create in ENVI
image= imread('rogue_29_2000.png');

%to see shape in Matlab
imshow(image);

% Create binary image or logical array
BW=im2bw(image,0.8);

% Flipping the conventions: Outside of the plume is black and the inside is
% white
BW_2= zeros(size(BW));
BW_2(BW==1)=0;
BW_2(BW==0)=1;

% Perimeter (used for the ellipse fitting)
BW_2_perim = bwperim(BW_2);
[roi.y,roi.x] = find(BW_2>0);
[roi.y_perim,roi.x_perim] = find(BW_2_perim);
roi.perim = length(roi.x_perim);

% ellipse fitting the perimeter using the function fit_ellipse_pca
ellipse = fit_ellipse_pca(roi.x,roi.y,0.9,1);
```



```

% fit_ellipse_pca
% method based on pca
function ellipse = fit_ellipse_pca(x,y,Q,illustration)

% Q is the only free parameter : the quantile used to compute ratio a/b of
the
% ellipse from the data points
%Q = 0.90;

centroid = [mean(x), mean(y)];
x_center = x - centroid(1);
y_center = y - centroid(2);

[coeff,~,~] = pca([x_center,y_center]);

% retrieve the tilt
theta = acos(coeff(1,1));
if coeff(2,1) < 0
    theta = -theta;
end

% I take all my data and I tilt them to match pc1-pc2 with x-y axis
xr = cos(-theta).*x_center - sin(-theta).*y_center;
yr = sin(-theta).*x_center + cos(-theta).*y_center;

% take a/b ratio as (x-axis maximal distance)/(x-axis maximal distance ratio)
a_min = quantile(xr,1-Q); a_max = quantile(xr,Q);
a = 0.5 * (a_max-a_min);
b_min = quantile(yr,1-Q); b_max = quantile(yr,Q);
b = 0.5 * (b_max-b_min);
axis_ratio = a/b;

% compute final a,b fixing area(ellipse) = area(plume)
a = sqrt(axis_ratio * length(x) / pi);
b = a / axis_ratio;

% angle between the river centerline and the major axis length
% major axis length
theta_2 = acosd(coeff(2,1));
if coeff(1,1) > 0
    theta_2 = -theta_2;
end

x1 = cosd(theta_2)*a + centroid(1);
y1 = abs(sind(theta_2)*a - centroid(2));

x2 = centroid(1) - cosd(theta_2)*a;
y2 = centroid(2) + sind(theta_2)*a;

X1P = [x1 x2];
X2P = [y1 y2];

% river centerline
X1RC = [500 205];

```

```

X2RC = [70 150];

% angle between river centerline and major axis
diff = (atan((X2P(1)-X2P(2))/(X1P(1)-X2P(1))) - atan((X2RC(2)-
X2RC(1))/(X1RC(2)-X1RC(1)))) * 180/pi;

ellipse = struct( ...
    'a',a,...
    'b',b,...
    'coeff',coeff,...
    'theta',theta,...
    'angle',diff,...
    'X0',centroid(1),...
    'Y0',centroid(2),...
    'status','ok' );

% illustration if desired
if illustration == 1

    % figure of the fit
    t = linspace(0,2*pi);
    xt = centroid(1) + cos(theta).*a.*cos(t) - sin(theta).*b.*sin(t);
    yt = centroid(2) + sin(theta).*a.*cos(t) + cos(theta).*b.*sin(t);
    figure; hold on; axis equal;
    plot(x,y,'b. ');
    plot(xt,yt,'r- ');
    line (X1P,X2P,'Color','k');
    line (X1RC,X2RC,'Color','g');
    legend('data','fit','Major-Axis','Riv-Centerline');
    set(gca,'Ydir','reverse');

    %figure of the overlap plume/ellipse area
    mask = ones(max(y),max(x));
    [y_im,x_im] = find(mask > -1);
    y_im = y_im - centroid(2);
    x_im = x_im - centroid(1);
    x_imr = cos(-theta).*x_im - sin(-theta).*y_im;
    y_imr = sin(-theta).*x_im + cos(-theta).*y_im;

    [y_plume,x_plume] = deal(y,x);
    y_plume = y_plume - centroid(2);
    x_plume = x_plume - centroid(1);
    x_plumer = cos(-theta).*x_plume - sin(-theta).*y_plume;
    y_plumer = sin(-theta).*x_plume + cos(-theta).*y_plume;

    overlap = zeros(size(x_imr));
    ellipse_only = zeros(size(x_imr));
    plume_only = zeros(size(x_imr));
    nothing = zeros(size(x_imr));

    for i=1:length(x_imr)

        is_in_plume = ~isempty(find(x_plumer==x_imr(i),1)) &&
~isempty(find(y_plumer==y_imr(i),1));
        is_in_ellipse = x_imr(i)^2/a^2 + y_imr(i)^2/b^2 <= 1;

```

```

    if is_in_plume && is_in_ellipse
        overlap(i) = 1;

    elseif is_in_plume
        plume_only(i) = 1;

    elseif is_in_ellipse
        ellipse_only(i) = 1;

    else
        nothing(i) = 1;

    end

end

% compute accuracy and F1 score based on confusion matrix of the overlap
accuracy = (sum(overlap(:)) + sum(nothing(:))) / length(x_imr);
F1 = 2*sum(overlap(:)) / (2*sum(overlap(:)) + sum(ellipse_only(:)) +
sum(plume_only(:)));

figure; hold on; axis equal;
plot(x_imr(overlap==1),y_imr(overlap==1),'g. ');
plot(x_imr(plume_only==1),y_imr(plume_only==1),'m. ');
plot(x_imr(ellipse_only==1),y_imr(ellipse_only==1),'r. ');
plot(x_imr(nothing==1),y_imr(nothing==1),'k. ');
title(sprintf('accuracy : %1.2f \t F1 : %1.2f \n',accuracy,F1));

end

```